

Evaluating a Downdraft Wood Fired Hydronic Furnace:  
Computational Fluid Dynamics Modeling and Analysis

Megan Karalus

A thesis submitted in partial fulfillment of the requirements for the degree of

Master of Science in Mechanical Engineering

University of Washington

2009

Program Authorized to Offer Degree: Mechanical Engineering



University of Washington  
Graduate School

This is to certify that I have examined this copy of a master's thesis by

Megan Karalus

and have found that it is complete and satisfactory in all respects,  
and that any and all revisions required by the final  
examining committee have been made.

Committee Members:

---

John Kramlich

---

James Riley

---

Ann Mescher

Date: \_\_\_\_\_



In presenting this thesis in partial fulfillment of the requirements for a master's degree at the University of Washington, I agree that the Library shall make its copies freely available for inspection. I further agree that extensive copying of this thesis is allowable only for scholarly purposes, consistent with "fair use" as prescribed in the U.S. Copyright Law. Any other reproduction for any purpose or by any means shall not be allowed without my written permission.

Signature\_\_\_\_\_

Date\_\_\_\_\_



## TABLE OF CONTENTS

	Page
List of Figures . . . . .	iii
List of Tables . . . . .	v
Chapter 1: Introduction . . . . .	1
1.1 Approaching the Problem . . . . .	4
1.2 Project Description . . . . .	6
Chapter 2: Literature Review . . . . .	8
Chapter 3: Fundamental Concepts . . . . .	10
3.1 Fuel Description . . . . .	10
3.2 Wood Combustion . . . . .	11
3.3 Heat Transfer . . . . .	18
3.4 Fluid Dynamics . . . . .	19
3.5 Combustion Theory and Modeling . . . . .	19
3.6 Turbulence . . . . .	21
Chapter 4: Benchmarking . . . . .	28
4.1 The Aspen . . . . .	28
4.2 Testing Methods and Results . . . . .	30
4.3 Benchmark Calculations . . . . .	35
Chapter 5: Slots Study . . . . .	42
5.1 Modeling Decisions and Initialization . . . . .	42
5.2 Results and Discussion . . . . .	50
Chapter 6: Conclusions and Recommendations . . . . .	65

Bibliography . . . . .	67
Appendix A: General Fuel Chemistry . . . . .	69
Appendix B: Orifice Calibration and Benchmarking . . . . .	71
Appendix C: Boundary Condition Calculations . . . . .	80

## LIST OF FIGURES

Figure Number	Page
1.1 Typical OWHH Configuration [1] . . . . .	2
1.2 Operation schematic of the Aspen . . . . .	5
3.1 A characteristic combustion lapse for one biomass particle [4] . . . . .	14
3.2 Schematics of fixed bed combustion, adapted from Hobbs [12] . . . . .	15
3.3 Schematic diagram of opposed flow flame spread . . . . .	17
3.4 Block Diagram of PDF lookup table creation [2] . . . . .	27
4.1 Operation schematic of the Aspen (repeated from Chapter 1) . . . . .	29
4.2 Air inlet passages and ports . . . . .	30
4.3 Typical discharge coefficient values and construction for an orifice meter [16] . . . . .	32
4.4 Gas mole fraction percentages from an EPA test Category 4 burn . . . . .	36
4.5 Category 4 discrete and continuous burn rate . . . . .	37
4.6 Excess air and equivalence ratio (surrogate fuel: CH <sub>2</sub> O) . . . . .	38
4.7 Stoichiometric Airflow (CFM) for 3 different surrogate fuel molecules . . . . .	40
4.8 Description of heat transfer at the fire brick surface . . . . .	41
5.1 PDF look up table . . . . .	48
5.2 Flame Structure - Contours of temperature on $Z_{stoich}$ iso-surface . . . . .	53
5.3 Velocities on a plane through Slot 4 for Grid 3 . . . . .	54
5.4 Contours of velocity through Slot 4 . . . . .	56
5.5 Stack species concentrations of test data vs. simulations . . . . .	60
5.6 Contours of CO mole fraction and the influence of secondary air . . . . .	62
5.7 Flame Structure - Contours of temperature on $Z_{stoich}$ iso-surface for sce- nario 2 without secondary air . . . . .	64
B.1 Vertical Velocity Profiles in the Orificed Duct . . . . .	73
B.2 Measurements and calculations for verification of the orifice coefficient of discharge . . . . .	76

B.3	Measurements and calculations for the inlet area flow rates in the furnace	77
B.4	Experimental data for weight burned vs. time during an EPA test, Category 4 burn	78
B.5	Baseline hand calculation of furnace air split	79
C.1	Relevant geometries (cross section of secondary chamber and chamber wall layers), and a description of heat transfer at the fire brick surface	81

## LIST OF TABLES

Table Number	Page
1.1 Energy sources for residential space heating . . . . .	1
3.1 Proximate and Ultimate Analysis of Wood Fuel . . . . .	10
3.2 Governing Equations Summary . . . . .	22
3.3 Favre Averaged Navier-Stokes Equations Summary [6] . . . . .	23
4.1 Total air flow rate into the furnace during combustion . . . . .	33
4.2 Flow split among air inlet ports . . . . .	34
4.3 Categories of Test Method 28 [24] . . . . .	35
5.1 Summary of computational grids . . . . .	46
5.2 Estimates for the composition of the pyrolysed fuel [13] . . . . .	47
5.3 Comparison of CO mole fractions at the top and bottom of each slot for three grid resolutions . . . . .	51
5.4 Comparison across three grids of the change in CO concentration through the slots . . . . .	57
5.5 Comparison of measured and calculated air flow rates . . . . .	57
5.6 Hand calculation of air split . . . . .	58
5.7 Comparison between simulation scenarios of CO mole fractions behavior in the slots . . . . .	63



## Chapter 1

**INTRODUCTION**

“Combustion and its control are essential to our existence on this planet as we know it” (Turns).

Combustion is responsible for producing a large percentage of the total energy consumed in the United States (e.g. internal combustion engines, gas-turbines, coal fired power plants, etc). It is also used on an individual scale with the most prevalent application being residential heating. As shown by the 2001 Department of Energy Survey given in Table 1.1 below, most households use natural gas or fuel oil if they are heating directly via combustion. We are interested in the other 3% who use wood, or more generically, biomass.

Table 1.1: Energy sources for residential space heating and the percentage of single-family US residences using each as their main heat source [17]

Fuel	Percentage
Natural Gas	60%
Electricity	23%
Fuel Oil	8%
Wood	3%
Other	6%

Fire places and wood stoves are common wood consumers, but neither of these produce much useful heat. Those who use wood or other biomass as a fuel for their primary

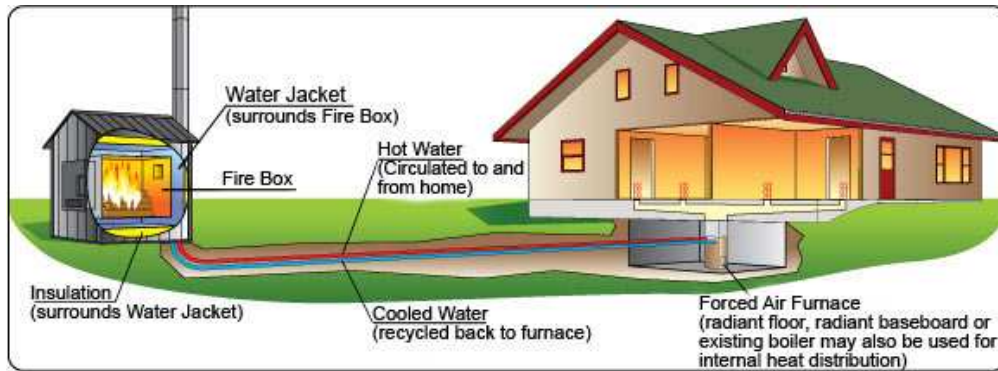


Figure 1.1: Typical OWHH Configuration [1]

heat source do so most commonly with a hydronic furnace also known as an outdoor wood-fired hydronic heater (OWHH). A typical configuration for a home system using an OWHH is shown in Figure 1.

Biomass is an increasingly popular fuel for a number of reasons. First, it has the potential to be “carbon neutral”, a statement carrying more weight as public concerns over CO<sub>2</sub> induced climate change grow. Second, biomass is a renewable fuel. More traditional fossil fuels like natural gas and fuel oil are a finite resource, the pace at which they are created by natural processes being orders of magnitude slower than the world’s growing consumption rate. Third and finally, biomass is a local resource. Tenuous relationships with countries holding the vast majority of the fossil fuel reserves is driving efforts to increase the use of ‘local fuels.’

As our use of combustion has grown, so has public concern over pollution. In 1955 the first Clean Air Act was passed. It has since been modified several times in the hopes that it will better protect public health and welfare. The current version of the Act requires EPA to establish National Ambient Air Quality Standards for six air pollutants although only three are of interest to biomass: nitrogen oxides (NO<sub>x</sub>), particulate matter (PM), and carbon monoxide (CO) [15]. Nitrogen oxides are formed in high temperature combustion environments and contribute to smog and the formation of acid rain. PM

and CO are both emissions of incomplete combustion. All of these pollutants can cause or aggravate respiratory conditions (asthma, bronchitis, etc), and lead to lung cancer, or cardiovascular issues. As Turns noted above, the art of controlling combustion is essential to our quality of life.

While the air standards above have caused the EPA to directly regulate coal fired power plants and other utility and industrial scale combustors, only recently have they adopted a certification program to curb emission from OWHHs. Although OWHHs produce NO<sub>x</sub>, CO, as well as PM, this voluntary program focuses only on PM emissions. For an OWHH to gain Phase II certification, its total particulate emissions must be less than 0.32 lbs per million BTU of heat output as measured by EPA's Test Method 28: *Measurement of Particulate Emissions and Heating Efficiency of Outdoor Wood-Fired Hydronic Heating Appliances*.

As demand for biomass fueled furnaces increases, in addition to their regulation, the OWHH industry is presented with three major technical challenges: (1) prevent harmful emissions (2) obtain high efficiency operation (3) expand capability for a broad range of fuels. Most of the existing units were designed via 'rules of thumb' and 'trial and error' methods. As the industry scales up however, they are interested in refining current designs - removing redundant and complex systems - and developing a deeper understanding of the operation of their units. This will help them to not only meet their technical challenges but also reduce the cost of the units.

Expanding to a wider variety of fuels such as wood chips and pellets means having a sound understanding of how various components of the furnace contribute to or detract from its current performance. This requires some modeling work, and unfortunately very little has been conducted for small wood/solid combustion furnaces for two basic reasons (1) solids combustion is a complex process not readily addressed in full in any commercial code (2) there was no previous motivation for it.

### ***1.1 Approaching the Problem***

The OWHH is designed to operate in a ‘batch-fire’ mode in which the fuel is reloaded every 8-12 hours. This is ideal from a consumer’s standpoint but problematic for the modeling engineer. Solids combustion typically consists of four distinct but overlapping stages:

1. Heating and Drying - Moisture is driven off and the outside of the fuel begins to approach pyrolysis temperatures.
2. Pyrolysis or Devolatilization - Heat from the flame is directed back towards the fuel, leading to its breakdown into pyrolysis fuel gas and solid carbon.
3. Combustion - The pyrolysis fuel gas mixes with the air and is burned in a buoyant diffusion flame. In this flame exist fine carbon particles, some from condensed fuel gas and others directly from the break down of the wood. Most of these burn out, but some escape, becoming PM emissions.
4. Char Oxidation - The solid carbon, left after all of the pyrolysis gasses have been driven off, reacts directly with oxygen from the air. This is the glowing char stage and does not produce significant smoke emissions.

There are two basic furnace configurations: updraft and downdraft, and while we will be examining a downdraft unit in this study it is important to understand the basic operation of both. In an updraft unit air is introduced near the bottom of the bed and combustion gasses move up through the bed. Over fire air is then added above the bed to induce mixing, breaking up large buoyant flame structures, and hopefully completing combustion. In a downdraft unit, air is introduced near the top of the bed and the emissions produced in the combustion zone are forced to pass down through the hot char oxidation region and into a secondary combustion chamber. For various reasons, downdraft units are inherently cleaner than their updraft counterparts and this will be discussed in detail in Chapter 3.

We now know in which stage most of the emissions are created, and that the key to low emissions is complete combustion. The three criteria for complete combustion are typically given as time, temperature, and turbulence (fuel/air mixing). The goal is to ensure that an adequate amount of air is mixed with the fuel gasses for a long enough period of time and the flame is maintained at a high enough temperature such that all of the particulate matter is oxidized. The mixing of air and fuel is in part controlled by the size of the flame, and the time needed to diffuse oxygen into a flame structure is proportional to the square of the structure size. Thus low emissions are served well by small flame structures.

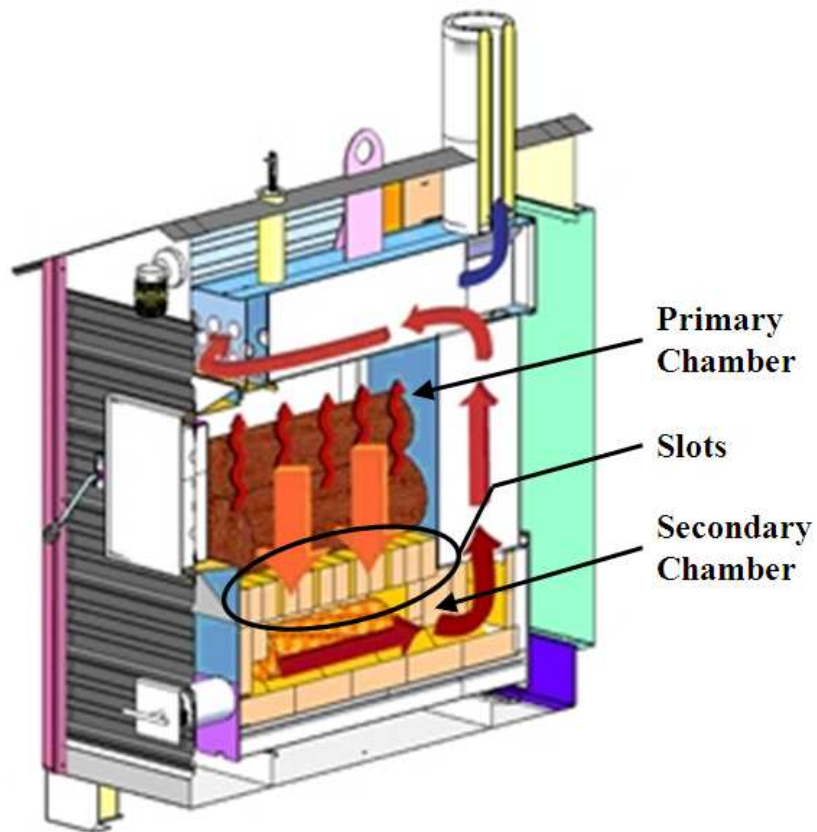


Figure 1.2: Operation schematic of the Aspen

The downdraft unit of interest is known as the Aspen and a schematic of its operation is shown in Figure 1.2. It already has excellent emission levels at 0.27 lbs per million BTU output, but like most OWHHs, it was designed using the ‘trial and error’ method and there is therefore little quantitative evidence for why it has such low emissions. In the current Aspen design, air is introduced in three areas: over the fuel bed, into the side of the fuel mass, and into the slots below the wood. The flame is forced through these slots which are intended to break up the flamelets and provide a confined space for introduction of secondary air in order to enhance mixing. The air path to the slots is quite complex however and difficult to manufacture. A significant cost savings results from not manufacturing the secondary air system, therefore the question to answer is whether or not this system is actually contributing to the unit’s low emissions. The goal of this research is to gain a quantitative understanding of how the Aspen accomplishes the goal of low emissions and to determine specifically if the secondary air introduction, which is intended to reduce emissions, is actually necessary.

## ***1.2 Project Description***

A full description of the solid combustion process in the OWHH is not yet practical. Because we are interested mostly in PM emissions, however, we have already narrowed the scope of the study, and based on general knowledge of wood combustion have reduced the problem to one of fluid dynamics. To explore the affect of the slots and secondary air injection on combustion emissions we first dissect the Aspen’s operation, determining the total air flow rate, the air flow split amongst the three areas of air introduction, and analyze EPA certified test data. This information is subsequently used to develop a Computational Fluid Dynamics (CFD) model of furnace operation during peak pyrolysis (peak PM emissions); FLUENT is the chosen CFD software. Modeling is conducted for two air flow scenarios (1) with secondary air and (2) without secondary air. The simulations are compared against the EPA test data, and significant analysis of combustion through the slots is performed using CO concentration as a metric for combustion

efficiency. Further justification for this approach is provided in Chapter 3.

## Chapter 2

### LITERATURE REVIEW

Most of the early research on fixed bed combustion focuses on energy production from coal. This is most evident in the extensive review of the technology and science related to fixed-bed systems completed by Hobbs. He states that “Combustion of coal in fixed-beds (e.g. stokers) is the oldest and historically the most common method of coal in use,” [12] and therefore the review focuses on coal as a fuel for these systems. This is important to the discussion of physical and chemical rate processes, but the operation of fixed bed systems can be extrapolated for general solid fuel particles of a similar size. He summarizes the features and assumptions of a large number of one and two dimensional models which cover countercurrent, cocurrent, and crosscurrent furnace configurations.

Due to growing concern over pollution and green-house gas emissions, literature coverage of fixed bed systems has moved towards energy production from biomass. Most of the work however has focused on processed fuels such as wood chips and biomass pellets. For instance Choi [5] and Yang [25] each developed packed bed combustion models for fuels with about a 10 mm diameter, equating to a Biot number near 1, in which they treated the bed as a continuous medium. While Choi’s and Yang’s work applied to up-draft units, Thunman produced a similar model for downdraft units (which he labels as countercurrent because the air flow and combustion front move in opposite directions) [20]. Peters developed a more comprehensive model that also considers each fuel particle’s individual combustion processes [18]. Even this model cannot accommodate a solid fuel as large as crib or cord wood however. In fact, describing the combustion process of a large solid fuel from first principles for use in a complete OWHH furnace simulation appears to be intractable at present.

We therefore look to models which approximate the solid combustion process such

that we can adequately describe the peak emissions of the furnace. A CFD tool for the analysis of combustion and emissions in batch-fired wood log combustion was given by Huttenen [13]. He identified the combustion of volatiles as the main source of PM emissions and therefore focused his modeling work on this combustion stage only, suggesting several pyrolysis gas compositions and various turbulence and reaction sub models. In general, the CFD calculations showed reasonable agreement with experimental results. He does note however that the models seemed to somewhat overestimate the overall efficiency of combustion (under-estimating CO in the exhaust gas). Huttenen's work was applied to a commercial updraft wood fired furnace by Glanville. The work produced similar agreement between CFD calculations and EPA certified tests of the furnace, and proved useful in suggesting furnace modifications for improved emissions [11]. The Slots Study of this thesis is largely based on the work of Huttenen and Glanville.

## Chapter 3

**FUNDAMENTAL CONCEPTS**

The goal of this work is to understand the affect of the slots and the secondary air on emissions from a downdraft wood fired furnace. In determining how to appropriately model the furnace for this purpose we must address four issues: (1) how to chemically characterize the ‘fuel’ during various stages of the burn, (2) how to accurately capture the physics of the flow field, (3) how to characterize heat transfer in the system, and (4) how to quantify emissions. The following section addresses the fundamental concepts necessary to make these modeling decisions.

**3.1 Fuel Description**

When considering wood combustion the most important properties of the fuel are the size, moisture content, elemental composition, and heating value. While some properties can vary with species, growth conditions, and location in the tree, simply specifying the species is enough for most combustion analyses.

Specifying a species sets the elemental composition and provides information on combustion matter content. This is determined in a similar fashion to coal, through ultimate and proximate analyses. Relevant information for the wood used in this study is shown in Table 3.1.

Table 3.1: Proximate and Ultimate Analysis of Wood Fuel

Species	Volatile Matter	Fixed Carbon	Ash	Elemental Weight Percentage			
				C	H	O	N
White Oak	86.2%	13.5%	0.3%	49.5	5.4	43.1	0.4

As a fuel for residential heating applications, wood is typically burned as cord wood because it requires the least amount of processing. Other types of wood fuel available include wood chips and wood pellets, with the latter being the most processed and uniform of the fuels. A third form of wood fuel, known as crib wood, is used mostly for testing purposes in place of cord wood because of its repeatability. Crib wood is used in the EPA Tests and therefore this is chosen for the modeling study. It should be noted however that the surface area to volume ratio of the fuel can have a significant impact on how combustion proceeds.

Finally the heating value of the dry wood is given as roughly 8,550 Btu/lb [11].

### 3.2 Wood Combustion

Here we will provide a review of wood combustion without considering the kinetics of specific reactions. It is divided into four basic stages (1) heating and drying, (2) devolatilization, (3) combustion, and (4) char oxidation.

#### 3.2.1 Heating and Drying

It is useful to introduce the two means of quantifying the moisture content of the wood as illustrated by Equations 3.1 and 3.2. The more common convention is moisture content on an oven-dry basis, and the less common on a wet, or green basis.

$$MC_w = \frac{m_{water}}{m_{wood,dry} + m_{water}} \quad (3.1)$$

$$MC_d = \frac{m_{water}}{m_{wood,dry}} \quad (3.2)$$

While it is easier to perform calculations on a wet basis we can easily convert between the two via Equation 3.3.

$$MC_d = \frac{MC_w}{1 - MC_w} \quad (3.3)$$

When the wood fuel is introduced to the preheated furnace, heating and drying begins quickly at the exposed wood surfaces and has three significant influences on the

combustion process. The first is to decrease the flame temperature and therefore the useful heat available [21]. For a 15° C wood sample with a 20% dry basis moisture content (typical for EPA method 28) the total heat required for drying is 426 kJ/kg (183 Btu/lb) which amounts to roughly 2% of the total heating value of dry wood [11]. The second is to place a ceiling on the temperature of the core of the fuel block until all of the water is vaporized. This may define reaction regions in the fuel. The third influence is to increase the thermal conductivity and heat capacity of the fuel block. Tillman provides equations for these properties based on moisture content [21].

### 3.2.2 *Devolatilization*

Pyrolysis of the wood produces the fuel for the type of ‘flaming combustion’ we are used to seeing in fire places. It does not involve reactions with oxygen. Rather, it is a solid-phase, chemical decomposition caused by heating. As a biomass, wood is composed of three basic organic polymer structures - cellulose, hemicellulose, and lignin - and each of these chemical structures undergoes thermal degradation to produce a number of volatile gasses. The solid phase pyrolysis products which consist of organic acids, aldehydes, esters, carbon dioxide, water vapor, and other species, diffuse through the outer char layer, enter the gas phase and break down into lighter more flammable species [11]. Tillman gives them to be CO, CO<sub>2</sub>, CH<sub>4</sub>, and C<sub>2</sub>H<sub>6</sub> and lists their relative percentages as 50, 10, 38, and 2 respectively [21]. Tars, which include numerous aromatic compounds, may also be a product of pyrolysis.

When the wood surface temperature reaches 500 K, solid phase pyrolysis begins. The temperature then climbs as pyrolysis proceeds, approaching an asymptote of 773 K (the maximum lignin pyrolysis temperature), until all of the volatiles are driven off and only char remains [21]. The rates and yields of pyrolysis are affected by a number of parameters, however including fuel composition, temperature, heating rate, and moisture content. Several kinetic models are suggested for wood pyrolysis by DiBlasi [7], however for the purposes of the Slots Study we are more interested in the volatile gas products

as a fuel for combustion.

In Huttenen's paper on emission formation during wood log combustion, two such models are suggested. The most basic is the single effective hydrocarbon gas proposed by Bhaskar [8]. To determine the formula of this gas we need only two pieces of information: (1) the volatiles and carbon content of the fuel, which from a proximate analysis we know to be approximately 80% and 20% respectively (2) the elemental composition of the fuel, which from an ultimate analysis of the fuel we know to be  $C_{4.12}H_{5.34}O_{2.70}N_{0.02}$ . With these the volatile molecule can be estimated to be  $CH_{2.12}O_{0.94}$ . For computational purposes Bhaskar approximated the fuel as formaldehyde,  $CH_2O$ . A heat of formation for the volatiles was found empirically by Bhaskar to be  $h_{f,CH_2O} = -276 \text{ MJ kmol}^{-1}$ .

The second volatile fuel model is based on experimental work done by Gronli. According to Gronli the pyrolysis fuel could be approximated as five species:  $CO_2$ ,  $CO$ ,  $CH_4$ ,  $H_2O$ , and  $H_2$ . The peak concentrations of these could be related as a molar ratio of  $HC : CO : CO_2 = 1 : 1.6 : 0.8$ . His experiments showed however that not all species reached their peak at the same time, in fact  $CO_2$  reached a peak concentration several minutes later than  $CO$  or  $HC$ . Therefore a second molar ratio of species was suggested,  $HC : CO : CO_2 = 1 : 1.6 : 0.4$  [13].

### 3.2.3 Combustion

The pyrolysis species now react with oxygen in the types of reactions important to combustion, e.g., radical chain branching. The combustion path proceeds as follows: first volatiles are cleaved into radical fragments, these radicals initiate the chain branching reactions of combustion, and then finally  $CO_2$  and  $H_2O$  are produced in chain termination reactions and radical recombinations. These final reactions are highly exothermic and responsible for most of the heat release. A full accounting of these gas phase reactions are given by Tillman [21]. In this discussion, Tillman notes the importance of the methyl and hydroxyl radicals to the progression of combustion and identifies the key combustion intermediate as  $CH_2O$ .

In this study we are particularly interested in the post combustion, or chain termination reactions in which CO is oxidized. Turns notes that CO is slow to oxidize unless there are some hydrogen containing species present because the CO oxidation step involving the hydroxyl radical is much faster than steps involving O<sub>2</sub> and O [22]. The pyrolysis gas approximations given above show substantial quantities of hydrogen which should lead to ample hydroxyl radical formation for complete and rapid CO oxidation.

### 3.2.4 Char Oxidation

Once the volatile matter has left the wood, only the glowing char remains. It is quite porous, containing numerous free-radical sites for O<sub>2</sub> to attack, however char combustion is much slower and lasts much longer than devolatilization and flaming combustion as shown in Figure 3.1.

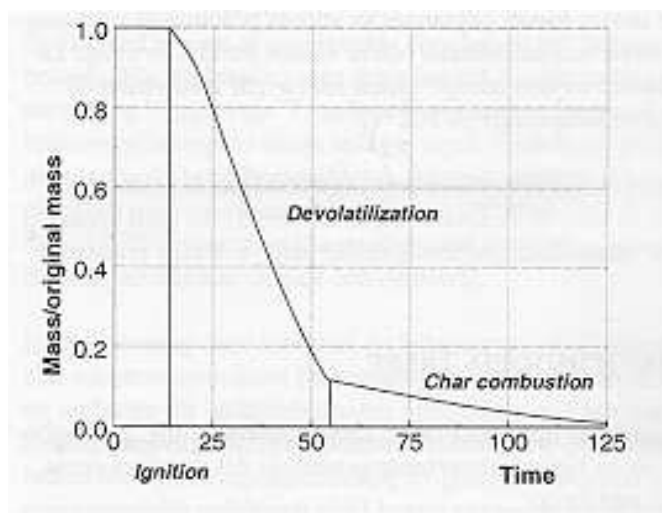


Figure 3.1: A characteristic combustion lapse for one biomass particle [4]

The location of these zones relative to each other is very important to furnace emissions, and schematics shown in Figure 3.2 illustrate the difference between updraft and downdraft combustors. In the downdraft design the combustion zone is located at or

near the top of the furnace, just below the devolatilization zone. Thus, all the volatiles released in pyrolysis are forced to pass through the hot char oxidation zone where they react with the char to produce clean combustible gasses [12].

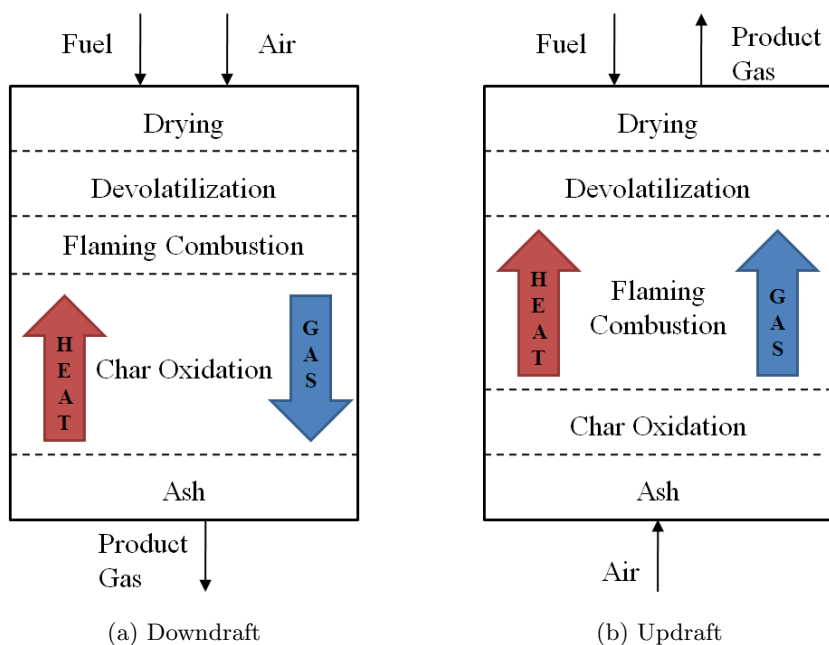


Figure 3.2: Schematics of fixed bed combustion, adapted from Hobbs [12]

### 3.2.5 Flame Behavior and PM Formation

Wood fire involves reactants (fuel and air) that are not mixed at the molecular level prior to combustion, therefore reactant mixing plays a vital role in characterizing the burning process. What results is a turbulent diffusion flame in which combustion chemistry is fast, and turbulent mixing is the slower, rate limiting process. Incomplete combustion products are more prevalent in this type of flame because of the non-uniformity of the mixture and temperature in the flame region. The shape of these turbulent diffusion flames is dictated by one of two forces: flames driven by momentum are known as

jet flames and are considered to be very ‘ordered’; flames with a low Froude number ( $Fr = u^2/gD \ll 1$ ) and thus low momentum flux tend to be buoyantly driven and more chaotic [6]. Wood fires fall under the last category.

The spread of a flame over the surface of a solid combustible is important to the study of a downdraft gasifier. This phenomenon is a function of heat transfer, chemical kinetics, and gas flow direction. For the flame to spread, enough heat must be transferred from the flame to the unburnt material ahead of the flame to pyrolyze the solid. The flame spread is then characterized as either opposed or concurrent depending on whether it is in the opposite or same direction as the flow of the oxidizer. In a downdraft combustor we have opposed flame spread. When the gas flow is in the direction of spread, the flame is pushed forward ahead of the pyrolysis region, which favors the transfer of heat that drives devolatilization of the unburnt material and results in fast spreading. On the other hand, when the gas flow opposes spread, the gas flow keeps the flame close to the surface of the solid downstream of the pyrolysis front resulting in a generally slow spread. In addition, experiments have shown that for all oxygen concentrations there is an initial region at low flow velocities where the flame spread rate is almost constant due to the buoyant entrainment of ambient gas by the flame [6].

Figure 3.3 shows the interaction of all combustion stages in flame spread. While flame spread is not included in the CFD model, this illustration speaks to the full physics of the solids combustion process.

### *Particulate Matter Formation*

Particulate matter (PM) emissions are divided into two categories by their composition and radiative properties: black carbon and brown carbon. Black carbon, more commonly known as soot, is an impure form of near-elemental carbon [3]. These particles exist in the wood flame, acting as a blackbody radiator to give the flame its yellow and red colors. Soot is usually formed on the fuel side of the reaction zone (fuel rich region) and is consumed when it meets an oxidizing region [22]. Soot only becomes an emission

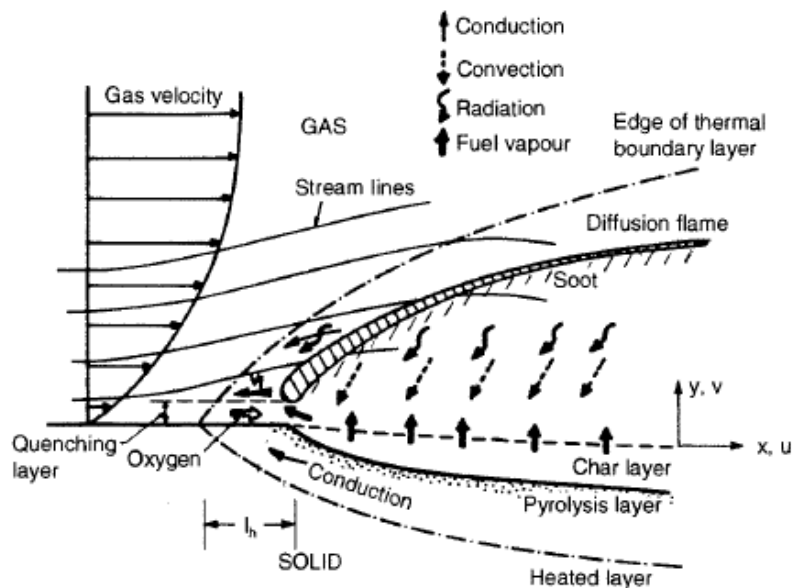


Figure 3.3: Schematic diagram of opposed flow flame spread over a solid [6]

when it breaks through the flame without being oxidized. Brown carbon, from biomass combustion, is composed of light-absorbing organic matter including condensed tars and amorphous, humic like substances. These originate in solid pyrolysis, escape the combustion flame, and then condense in the cooling plume [3].

A study done by Fine [10] indicated that for general fire place wood combustion, particulate emissions were composed mostly of brown carbon. For a test using Northern Red Oak, a close relative of the White Oak used in this study, Fine found that 90% of the PM emissions were from organic carbon (brown carbon) and only 4% from elemental carbon (black carbon). This is very important in addressing the modeling of PM formation. First, there is no PM emissions model grounded in physics that is not semi-empirical. Second, the semi-empirical models that are found in the literature predict soot, or black carbon formation only, and the empirical constants derived are based on steady state, momentum driven, light hydrocarbon flames [11]. This is in almost complete opposition

to the characteristics of a wood fired downdraft combustor whose main PM emission is brown carbon and whose flames are chaotic, transient, and buoyantly driven. Therefore a review of these soot models will not be undertaken and their use in the slots modeling study will not be included.

### 3.3 Heat Transfer

Heat transfer is inherently important to the combustion processes and none of the three forms of heat transfer: conduction, convection, and radiation, may be ignored. Convection is essential to the preheating of the inlet air and heat transfer to the water jacket, which is the purpose of the OWHH. Since heat must flow in the opposite direction of the gasses in a downdraft combustor, radiation and conduction are responsible for driving pyrolysis. (In the slots study this is not addressed because a kinetic model for pyrolysis is not used).

The well known classical relationships for the three heat transfer modes are Fourier's Law of Heat Conduction (1-D), Newton's Law of Cooling, and the Stefan-Boltzmann Law which, and these are given by Equations , , and [14]. The radiation and convection equations are given for surface heating which is often the case in the OWHH, however gas radiation from the combustion products, CO<sub>2</sub> and H<sub>2</sub>O, will also be important. Methods for determining the phenomenological parameters  $\epsilon$ ,  $k$ , and  $h$  are discussed in the sections on benchmark calculations and modeling.

$$q''_{cond} = -k \frac{\partial T}{\partial x} \quad (3.4)$$

$$q''_{conv} = h(T_{\infty} - T_s) \quad (3.5)$$

$$q''_{cond} = \epsilon \sigma_b (T_{\infty}^4 - T_s^4) \quad (3.6)$$

### 3.4 Fluid Dynamics

The fluid flow in the Aspen furnace may be completely described by the Navier-Stokes Equations of mass and momentum conservation given by Equations 3.7 and 3.8. Compared with non-reacting flows, reacting flows are subject to large density gradients. Therefore both of the density gradient terms in the continuity and momentum equations are retained along with the second term in the stress tensor definition: the “dilatational expansion” momentum sink [11]. The equations are given in index form and the momentum equation retains the gravitational body force to account for buoyancy effects. Despite the density gradients, the flow can still be treated as incompressible for two reasons (1) the density gradients are not pressure induced, and (2) the ideal gas law is still a good approximation for the hot combustion gasses in the furnace.

$$\frac{\partial \rho}{\partial t} + \frac{\partial}{\partial x_j} (\rho u_j) = 0 \quad (3.7)$$

$$\frac{\partial}{\partial t} (\rho u_i) + \frac{\partial}{\partial x_j} (\rho u_i u_j) = -\frac{\partial P}{\partial x_j} + \frac{\partial \tau_{ij}}{\partial x_j} + \rho g_i \quad (3.8)$$

$$\tau_{ij} = \mu \left( \frac{\partial u_i}{\partial x_j} + \frac{\partial u_j}{\partial x_i} \right) - \frac{2}{3} \mu \frac{\partial u_k}{\partial x_k} \delta_{ij} \quad (3.9)$$

As noted earlier the fire of this study may be thought of as a buoyantly driven diffusion flame and despite its lazy nature and moderate Reynolds numbers it is often fully turbulent. In the absence of a strong momentum flux, density gradients cause instabilities that can either aid or inhibit reactant mixing, thermal transport, local turbulence, and flame quenching. Therefore understanding and properly modeling the flow field will be of paramount importance.

### 3.5 Combustion Theory and Modeling

To incorporate the gas phase combustion discussed above into a complete fluid dynamic description of the system we need to include two more equations. The first is conservation

of energy expressed in terms of the mixture static enthalpy. Equation 3.10 accounts for energy transportation due to advection, conduction, and radiation as well as enthalpy and pressure changes with time. This form of the energy equation is developed using a series of assumptions based on the usually low velocities of fires. This implies that the viscous dissipation of enthalpy, work due to buoyancy forces, and the heat flux due to concentration gradients can all be neglected, in addition to the mixture kinetic energy which is small when compared with mixture enthalpy. The static enthalpy of this equation is given as  $h = C_p T + \sum_{\alpha} X_{\alpha} H_{\alpha}$  where  $C_p$  is a local mass weighted average and  $H_{\alpha}$  is the enthalpy of formation of the species  $\alpha$  [6]. Finally, assuming that thermal and species diffusivities are equal (unit Lewis number), which is a common and reasonable assumption for most complex combustion flow treatments, the last of the conservation equations can be derived. The unit Lewis number decouples this last equation for chemical species from the energy equation.

$$\frac{\partial}{\partial t} (\rho h) + \frac{\partial}{\partial x_j} (\rho u_j h) = \frac{\partial P}{\partial t} + \frac{\partial}{\partial x_j} \left[ \frac{k}{C_p} \frac{\partial h}{\partial x_j} \right] - \dot{q}_j^R \quad (3.10)$$

Species conservation given by Equation 3.11 accounts for mean flow advection, Fickian Diffusion, and a chemical reaction source term.

$$\frac{\partial}{\partial t} (\rho X_{\alpha}) + \frac{\partial}{\partial x_j} (\rho u_j X_{\alpha}) = \frac{\partial}{\partial x_j} \left( \rho D \frac{\partial X_{\alpha}}{\partial x_j} \right) + S_{\alpha} \quad (3.11)$$

Hydrocarbon combustion involves complex mechanisms, with many reaction pathways and species. Current research on methane combustion alone considers 277 elementary reactions with 49 species [22]. For each species considered, a conservation equation is necessary and the complexity of the system's solution increases very quickly. For our case, even if we only consider global reactions for pyrolysis species listed earlier (CO, CO<sub>2</sub>, H<sub>2</sub>, H<sub>2</sub>O, CH<sub>4</sub>, and O<sub>2</sub>), we still need an additional six species conservation equations, requiring the simultaneous solution of a total of nine differential equations for the system.

### 3.5.1 Mixture Fraction

The mixture fraction approach allows us to consolidate the six species conservation equations into one conservation equation of a scalar: mixture fraction, often denoted as  $Z$ . Mixture fraction is defined by Equation 3.12 such that it is equal to 1 in the fuel stream and 0 in the oxidizer stream [19]. In this approach the system is treated as having infinitely fast chemistry, therefore “mixed is burned” because fuel and oxidizer cannot coexist without reacting. Under the assumption of equilibrium chemistry the mixture fraction can be directly related to other scalars (density, temperature, etc) resulting in further simplification of the solution. The mixture fraction approach has been specifically developed for turbulent diffusion flames in which turbulent mixing is the rate limiting process as discussed earlier [2].

$$Z = \frac{m_{fuel}}{m_{fuel} + m_{oxidizer}} \quad (3.12)$$

The conservation of the mixture fraction is expressed by Equation 3.13 assuming equal diffusivities among species and a unity Lewis number [11]. Coupling mixture fraction to the turbulence model will be discussed in Section 3.6.2.

$$\frac{\partial}{\partial t} (\rho Z) + \frac{\partial}{\partial x_j} (\rho u_j Z) = \frac{\partial}{\partial x_j} \left( \rho D \frac{\partial Z}{\partial x_j} \right) \quad (3.13)$$

## 3.6 Turbulence

So far we have derived governing equations for the furnace system with few approximations, including equations for the conservation of mass, momentum, energy, and mixture fraction. We noted earlier however that the flame of an OWHH is inherently turbulent due to the effects of buoyancy. The most accurate approach to turbulence simulation is to solve the Navier-Stokes equations given in Table 3.2 directly, referred to as Direct Numerical Simulation (DNS). A valid simulation must capture all turbulent scales requiring that the grid size scale with the Reynolds number as  $Re_L^3$ , thus this method

is too computationally expensive for most practical engineering problems. Instead we employ a turbulence model, the most typical one being proposed by Osborn Reynolds over a century ago in which we assume a statistically steady flow and average all of the unsteadiness out. The result is the set of Reynolds-Averaged Navier-Stokes (RANS) equations. On averaging these equations a ‘closure problem’ is introduced and this has been addressed by numerous models relying by various degrees on empiricism, intuition, and physical arguments, all of which should be regarded as engineering approximations [19] [9].

Table 3.2: Governing Equations Summary

Equation Name	Equation
Continuity	$\frac{\partial \rho}{\partial t} + \frac{\partial}{\partial x_j} (\rho u_j) = 0$
Momentum	$\frac{\partial}{\partial t} (\rho u_i) + \frac{\partial}{\partial x_j} (\rho u_i u_j) = -\frac{\partial P}{\partial x_i} + \frac{\partial \tau_{ij}}{\partial x_j} + \rho g_i$
Energy	$\frac{\partial}{\partial t} (\rho h) + \frac{\partial}{\partial x_j} (\rho u_j h) = \frac{\partial P}{\partial t} + \frac{\partial}{\partial x_j} \left( \frac{k}{C_p} \frac{\partial h}{\partial x_j} - \rho u_j' h' \right) - \frac{\partial \dot{q}_j^R}{\partial x_j}$
Mixture Fraction	$\frac{\partial}{\partial t} (\rho Z) + \frac{\partial}{\partial x_j} (\rho u_j Z) = \frac{\partial}{\partial x_j} \left( \rho D \frac{\partial Z}{\partial x_j} \right)$

To begin the turbulence modeling we must decompose the variables  $\rho$ ,  $u$ ,  $h$ , and  $Z$  into averaged and fluctuating components. Due to the large density gradients in the furnace, density averaged variables will be used instead of the strictly time averaged values of RANS. These forms of the equations are referred to as the Favre-Averaged Navier-Stokes (FANS) equations. The decomposition and density averaging of a generic variable  $\Phi$  is given by Equations 3.14 and 3.15 where  $\tilde{\Phi}$  is the density-weighted time average of the variable and  $\bar{\Phi}$  is the Reynolds, or simply time averaged quantity. (Note that  $\overline{\rho\Phi} = \bar{\rho}\tilde{\Phi}$ .)

$$\Phi(x, t) = \tilde{\Phi}(x, t) + \Phi'(x, t) \quad (3.14)$$

$$\tilde{\Phi}(x, t) = \frac{\int_T \rho(x, t) \Phi(x, t) dt}{\int_T \rho(x, t) dt} = \frac{\overline{\rho \Phi}}{\bar{\rho}} \quad (3.15)$$

The decomposed variables are substituted back into the original equations given by Table 3.2 and the Favre Averaged Equations are born. The resulting equations are summarized by Table 3.3, although mixture fraction is omitted for the moment because turbulent chemistry interaction will be addressed in the following section.

Table 3.3: Favre Averaged Navier-Stokes Equations Summary [6]

Equation Name	Equation
Continuity	$\frac{\partial \bar{\rho}}{\partial t} + \frac{\partial}{\partial x_j} (\bar{\rho} \tilde{u}_j) = 0$
Momentum	$\frac{\partial}{\partial t} (\bar{\rho} \tilde{u}_i) + \frac{\partial}{\partial x_j} (\bar{\rho} \tilde{u}_i \tilde{u}_j) = -\frac{\partial \bar{P}}{\partial x_i} + \frac{\partial}{\partial x_j} \left( \bar{\tau}_{ij} - \overline{\rho u'_i u'_j} \right) + \overline{\rho g_i}$
Energy	$\frac{\partial}{\partial t} (\bar{\rho} \bar{h}) + \frac{\partial}{\partial x_j} (\bar{\rho} \tilde{u}_j \bar{h}) = \frac{\partial P}{\partial t} + \frac{\partial}{\partial x_j} \left( \frac{k}{C_p} \frac{\partial \bar{h}}{\partial x_j} - \overline{\rho u'_j h'} \right) - \frac{\partial \dot{q}_j^R}{\partial x_j}$

While the equations of Table 3.2 are a closed system when they are combined with the ideal gas law, the equations of Table 3.3 are not and still contain fluctuating quantities ( $\Phi'$ ) known as turbulent transport terms. The closure of this system of equations requires a turbulence model based usually on some approximations for the Reynolds stress tensor and turbulent scalar fluxes.

No turbulence model is universally accepted as being superior for all problems, therefore in choosing a model we must consider the physics of the flow field, the accuracy required, and the computational ‘budget’ available. The most computationally expensive and elaborate model is the Reynolds Stress Model in which seven additional transport

equations are solved for the individual Reynolds stresses [2][9]. It has several advantages but also many limitations and a simpler model requiring only two additional transport equations may serve just as well. In this study we will examine the  $k - \varepsilon$  model.

### 3.6.1 The $k - \varepsilon$ Model

The importance of viscosity in defining the behavior of laminar flows is well established, therefore we begin our turbulence model by assuming that the effect of turbulence can be represented as an increased viscosity. Using the Boussinesq Approach, the Reynolds stresses can be modeled with this new turbulent viscosity as shown in Equation 3.16 where  $k$  is defined as the turbulent kinetic energy (Equation 3.17) [19].

$$-\overline{\rho u'_i u'_j} = -\bar{\rho} \widetilde{u'_i u'_j} = \bar{\rho} \nu_t \left[ \left( \frac{\partial \tilde{u}_i}{\partial x_j} + \frac{\partial \tilde{u}_j}{\partial x_i} \right) - \frac{2}{3} \frac{\partial u_k}{\partial x_k} \delta_{ij} \right] - \frac{2}{3} \delta_{ij} \bar{\rho} \tilde{k} \quad (3.16)$$

$$k = \frac{1}{2} \widetilde{u'_i u'_j} \quad (3.17)$$

According to Ferziger, the simplest characterization of turbulence requires two parameters: kinetic energy,  $k$ , and a length scale,  $L$ . An exact equation for the turbulent kinetic energy can be derived, and it naturally includes transport, production, and dissipation terms. All of these terms require some extent of modeling, but the turbulent dissipation term will require the solution of a separate equation. Unfortunately, an accurate prescription of  $L$  is only possible for simple flows, and therefore another equation is also required to determine this quantity.

The most popular turbulence model, the  $k - \varepsilon$  model, assumes an equilibrium turbulent flow (one in which the rates of production and destruction of turbulence are in near-balance) and therefore  $\varepsilon$ ,  $k$ , and  $L$  can be related by Equation 3.18.

$$\varepsilon \approx \frac{k^{3/2}}{L} \quad (3.18)$$

This allows the use of one equation, for  $\varepsilon$ , to determine both  $\varepsilon$  and  $L$ , and the

turbulent kinematic viscosity for the Favre averaged Navier-Stokes equation above can then be expressed as:

$$\nu_t = C_\mu \frac{\tilde{k}^2}{\varepsilon} \quad (3.19)$$

Although exact equations for dissipation can be derived from the Navier-Stokes equations, severe modeling is necessary and therefore the entire equation should be thought of as an empirical model [9]. In fact FLUENT, the CFD software program chosen for the Slots Study, provides three  $k - \varepsilon$  options: Standard, RNG, and Realizable, each of which approaches the modeling of turbulent dissipation differently. The mathematical difference among the three will not be discussed here.

For the purposes of this study however, the Realizable model was chosen. Initially, the RNG model was used, however turbulent viscosity ratios in some flow regions began to approach infinity and had to be artificially limited during the runs. This tended to occur in recirculation zones in the open furnace cavity. To prevent this, the realizable model was chosen because it is “likely to provide superior performance for flows involving rotation..., separation, and recirculation” [2]. According to the FLUENT documentation, this is because the model satisfies certain mathematical constraints on the Reynolds stresses that are consistent with the physics of turbulent flows. This is most evident in the determination of the constant  $C_\mu$ . In the standard and RNG formulations  $C_\mu \approx 0.09$ , but under the Realizable model  $C_\mu$  is made variable, dependent on the mean flow and turbulence and ranging from approximately 0.09 in the inertial sub layer to 0.05 in strong homogeneous shear flow [2].

It should be noted that inherent to the  $k - \varepsilon$  model is its assumption of isotropic turbulence. This is not problematic at smaller scales, but is in capturing larger buoyancy induced turbulent structures.

### 3.6.2 Turbulence Chemistry Interactions

As noted previously, chemistry modeling can be simplified by solving only one equation for a conserved scalar rather than an individual conservation equation for each species. Under the assumption of chemical equilibrium the instantaneous mixture fraction is related to species fractions, density, and temperature in the system. When turbulence is introduced and instantaneous values are ‘averaged’ for turbulence modeling, a turbulence-chemistry interaction model is necessary.

To account for fluctuations in the flow field, mixture fraction is typically applied with the assumed-shape probability density function or PDF approach. The PDF represents the fraction of time that a fluid spends in the vicinity of  $Z$  [2]. In practice the PDF is unknown and is modeled as a mathematical function that approximates what has been observed experimentally. The most common assumed-shape PDF is the  $\beta$ -Function. Like the normal distribution it can be characterized by its mean  $\bar{Z}$  and its variance  $\overline{Z'^2}$ . It is defined as follows:

$$p(Z) = \frac{Z^{\alpha-1}(1-Z)^{\beta-1}}{\int Z^{\alpha-1}(1-Z)^{\beta-1}dZ} \quad (3.20)$$

where

$$\alpha = \bar{Z} \left[ \frac{\bar{Z}(1-\bar{Z})}{\overline{Z'^2}} - 1 \right] \quad (3.21)$$

and

$$\beta = (1-\bar{Z}) \left[ \frac{\bar{Z}(1-\bar{Z})}{\overline{Z'^2}} - 1 \right] \quad (3.22)$$

Our combustion system is not adiabatic and therefore temperature, species fractions, and density are dependent on enthalpy as well as mixture fraction. In such systems turbulent fluctuations should be accounted for by a joint PDF  $p(Z, H)$ . This is computationally expensive however, and there is a simpler alternative if we assume that heat losses do not significantly impact the turbulent enthalpy fluctuations. A lookup table dependent on three variables - mixture fraction  $\bar{Z}$ , mixture fraction variance  $\overline{Z'^2}$ , and scaled heat flux ( $\bar{H}$ ) - is created for the scalar values of interest [2]. A block diagram illustrating the table creation is shown in Figure 3.4.

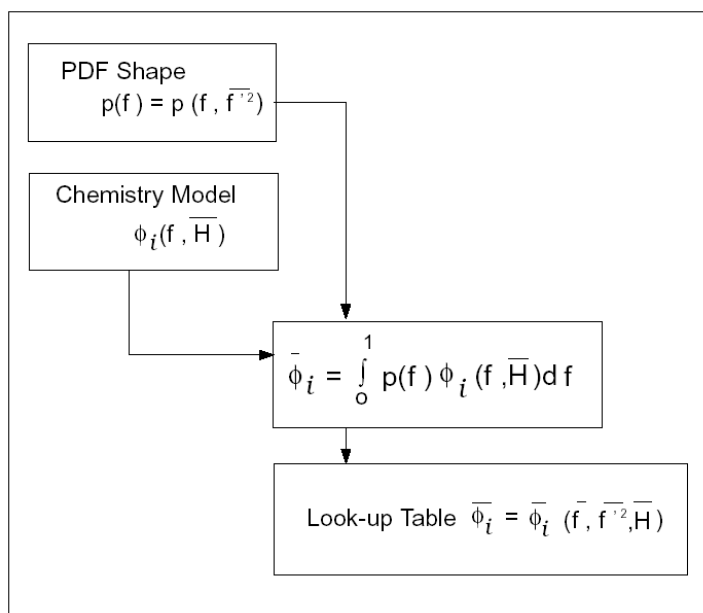


Figure 3.4: Block Diagram of PDF lookup table creation [2]

## Chapter 4

**BENCHMARKING****4.1 *The Aspen***

We now introduce the case study furnace used for modeling and analysis. The Aspen is a simple furnace that uses water, warmed via biomass (currently wood) combustion, for space heating applications. The principle of operation of the Aspen furnace is shown in Figure 4.1. Wood in the primary chamber burns from the bottom up, while forced air drives the combustion gasses down through the burning bed and into the secondary burn chamber. Secondary air is added as the gas passes through the four slots separating the two chambers. Exhaust then travels through a series of fire tubes where heat is exchanged between the flue gasses and the water in the jacket before it is released to the environment through the stack. The Aspen's water jacket is an enclosed water filled space surrounding all four sides of the primary chamber, the door, and the fire tubes. Natural convection is responsible for circulating the water in the jacket until it reaches the desired application temperature. The jacket around the primary chamber walls and the door insulates the unit to prevent skin losses and maintains safe external surface temperatures. Heat output of the unit is controlled by metering the burn through a damper plate over the air inlet.

Two important aspects of the Aspen design include the use of fire clay brick in the primary and secondary chambers, and the air distribution among the combustion zones. The fire clay brick in the Aspen acts as a thermal insulator, thermal mass, and re-radiator, maintaining high temperatures in the secondary chamber and at the bottom of the wood bed in the primary chamber. While generally speaking, air is introduced in the Aspen in a top down approach, there are actually three introduction areas and

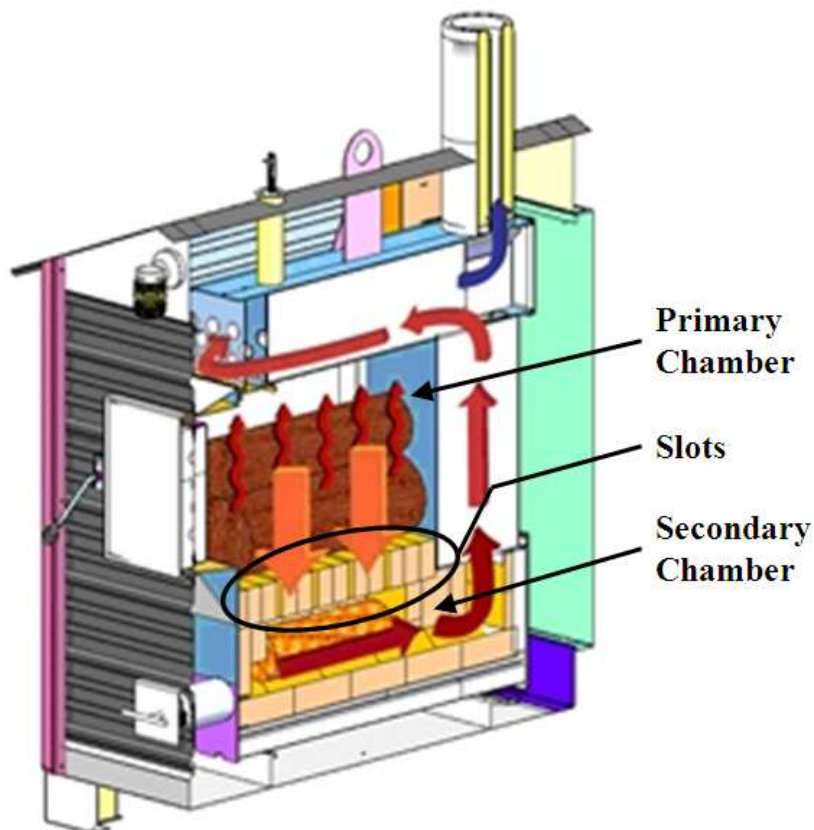


Figure 4.1: Operation schematic of the Aspen (repeated from Chapter 1)

seven ports. Figure 4.2 shows the design in detail. The passageways to the side and secondary ports are formed by the fire clay brick layout while the path to the top port is part of the steel walled water jacket. These pathways allow for some air preheating before introduction into the burn chambers. A single fan feeds all seven ports and the division of air among the areas is unknown.

Three variables control the emissions of the furnace: temperature, mixing, and air quantity and distribution. Determining both the total air flow to the furnace and the distribution of air among the inlet ports is essential to understanding the combustion process that contributes to low emissions.

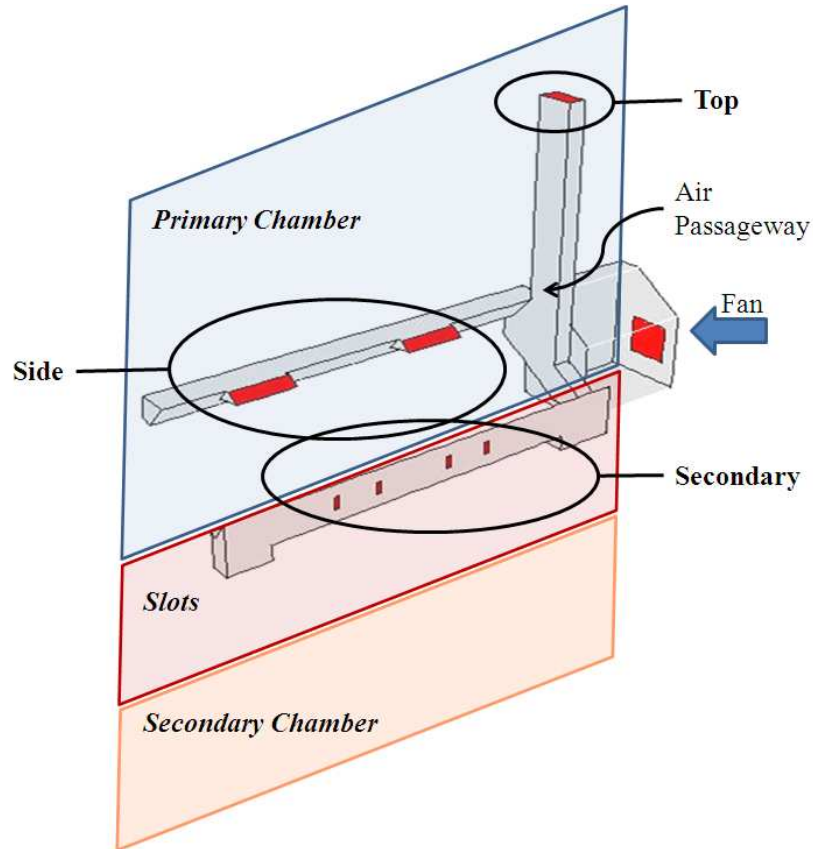


Figure 4.2: Air inlet passages and ports

## 4.2 Testing Methods and Results

In order for modeling to proceed we must quantitatively characterize the operation of the Aspen. This includes looking at the total air flow, the air split among the three inlet areas, the burn rate, the fire brick temperature, the water jacket temperature, and the exhaust gas makeup. All of these will be addressed by the following test methods, results, and theoretical calculations.

#### 4.2.1 Air Flow Measurements

Two types of air flow measurements were taken on the Aspen furnace. First we wished to know the total air flow to the furnace and this was easily accomplished using a simple orifice meter. Second, we needed to determine how the total volumetric flow to the furnace split among the three inlet areas. This was determined by calculating a flow rate through each port using velocities measured with a pitot tube and some assumptions regarding the port's velocity profile.

##### *Tools and Set-up*

The orifice was constructed in-house by inserting a flat plate with a hole between two flanges of a duct. Typical set-up to determine the total furnace flow rate placed the duct on the inlet side of the fan (i.e. the fan drew air through the duct and blew it into the furnace).

The flow rate across the orifice is determined using Equation 4.1 derived from the application of Bernoulli's equation between two points [16]. Here  $\beta = d/D$ ,  $\Delta P$  is the pressure difference between the taps,  $A_0$  is the area of the orifice, and  $C_0$  is the discharge coefficient that accounts for non-ideal effects (turbulence, vena contracta, etc).

$$Q = C_0 A_0 \sqrt{\frac{2\Delta P}{\rho(1 - \beta^4)}} \quad (4.1)$$

The value of  $C_0$  is a function of  $\beta$  and the Reynolds number as well as the placement of the pressure taps and the construction of the orifice plate. Typical discharge coefficient values for the given orifice construction are shown in Figure 4.3. A pipe diameter of 6 inches, an orifice diameter of 3 inches and a Reynolds number of  $1.5 \times 10^4$  suggests a  $C_0$  of 0.61. Because the orifice meter was constructed in house however we determined the  $C_0$  experimentally. Using the set-up and method outlined in Appendix B,  $C_0$  was found to be 0.54 and this is the value used for all total flow measurements in the furnace.

The second air flow measurement, air flow speed, was made using a pitot tube. The pressure measured at the pitot tube's tip is the stagnation pressure and this is related

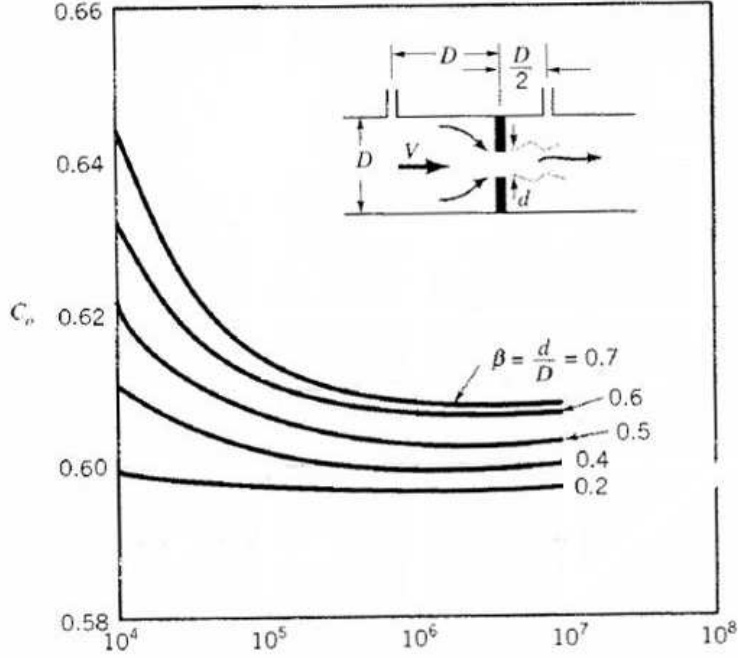


Figure 4.3: Typical discharge coefficient values and construction for an orifice meter [16]

to the upstream velocity through Bernoulli's equation

$$P_n = P_{\text{static}} + \frac{\rho V^2}{2} \quad (4.2)$$

where  $P_n$  is the stagnation pressure at the point of interest,  $P_{\text{static}} \approx P_{\text{atm}}$  which is atmospheric pressure, and  $\rho$  is the density of air.

Velocity measurements were taken in each port and volumetric flow rates calculated from them. In the top port and secondary ports, a flat turbulent profile was assumed so only one measurement was taken in the center of each. For the side ports however, we took three measurements along their lengths because of the sharp elbows immediately preceding the air's entrance to the furnace cavity. These are referred to as 'front', 'center', and 'back' with 'front' meaning closest to the furnace door. It was assumed that the front and center velocities were each averaged over 40% of the port's area and the back

accounted for 10%.

Two sets of measurements were taken to ensure adequate repeatability. Further information regarding these measurements and calculations can be found in Appendix B.

### *Results*

Using the experimentally derived discharge coefficient and orifice pressure tap readings from furnace tests we easily found the total flow rate to the furnace as given in Table 4.1.

Table 4.1: Total air flow rate into the furnace during combustion

$C_0$	$\Delta P$ (in $\text{H}_2\text{O}$ )	Total Air Flow Rate (CFM)
0.54	0.38	61.7

Results from the second air flow measurement are shown in Table 4.2. It is evident from comparing the total CFM values from these tests to that determined by the orifice that the velocity profile assumptions for the air ports are not accurate. It is assumed however that while these measurements are not accurate on an absolute scale, the average percent distribution can be used with the orifice flow rate measurement to determine an adequate approximation of the proper air split.

#### *4.2.2 EPA Method 28*

The EPA Test Method 28 is used to measure the particulate emissions and heating efficiency of an outdoor wood-fired hydronic furnace. While in the Slots Study we use carbon monoxide as an indicator of PM emissions, all benchmark testing was conducted using this method and its fuel specifications are important for subsequent modeling.

Per Method 28 requirements, the test crib is composed of  $4'' \times 4''$  pieces of White Oak, that are 80% of the longest firebox dimension in length, this being approximately

Table 4.2: Flow split among air inlet ports

	<i>Test 1</i>	<i>Test 2</i>	
<i>Inlet Areas</i>	<b>Total CFM 79.4</b>	<b>Total CFM 86.9</b>	<b>Average</b>
<b>Top</b>	55%	59%	57%
<b>Side</b>	42%	39%	40%
<b>Secondary</b>	3%	2%	3%

16 inches for the Aspen. The number of crib pieces is determined by the firebox volume, the total crib weight being 10 lbs/ft<sup>3</sup> of firebox space. For the Aspen this is 100 lbs, or 9 crib pieces. The crib pieces are held together by 3/4 inch spacers. The fuel must have a moisture content of 19 – 25% on a dry basis which is determined by a hand held electric resistance moisture meter. The moisture content in a crib piece is not uniform throughout so an average of at least three points, 3 inches from each of the ends and parallel to the grain, is used. The reasoning behind using crib pieces instead of cord wood is the repeatability of the test. The fuel crib eliminates irregularities in surface area, geometry, bark content, etc.

Many measurements are taken as the test progresses including: the weight change of the furnace in lbs, the stack temperature and static pressure, the inlet (cold) and outlet (hot) temperatures of the heat transfer loop, Particulate Matter (PM) emissions (lbs/MMBtu), and constituent concentrations of the exhaust gas. To make these measurements the method calls for using a scale ( $\pm 1.0$  lb), thermocouples, a static-pitot tube, PM sampling train as per EPA Method 5G [23], and a dry gas meter to measure the mole fractions of CO and CO<sub>2</sub>. To complete Method 28 the furnace must be run under four energy output conditions, each referred to as a different burn category. The total PM emissions for the furnace is then calculated using all four scenarios. The category definitions and weighting factors are given in Table 4.3.

The most important of these for our modeling purposes are the weight change, used to

Table 4.3: Categories of Test Method 28 [24]

Category	Percentage of Maximum Rated Output	Year-Round Weighting Factors	Seasonal Weighting Factors
1	< 15%	0.437	0.175
2	16 to 24%	0.238	0.275
3	25 to 50%	0.275	0.450
4	100%	0.050	0.100

determine the burn rate, and the dry gas meter measurements, used for the stoichiometry calculations. The burn rate for categories 1 through 3 is controlled using a damper plate on the air inlet. Category 4 generally runs at full output and does not need the damper plate to be activated. This keeps the flow field, pyrolysis, and flame dynamics closer to steady state and therefore data from this run only will be used for the benchmark calculations. Dry gas meter results for a Category 4 burn are shown in Figure 4.4

While measuring the combustion temperature of the secondary chamber is not part of the EPA test method, this measurement was added to the Category 4 burn and used to calculate the fire brick temperature as detailed Section 4.3.3.

### 4.3 Benchmark Calculations

#### 4.3.1 Burn Rate

During the EPA tests the mass loss of the furnace is measured and recorded on 10 minute intervals. This is low resolution data and as can be seen from Figure 4.5 the discrete burn rate calculated directly from these measurements is very course. To ‘smooth’ the data, a fourth order polynomial fit of weight burned vs. time was used. This plot and the polynomial equation are given in Appendix B. The burn rate taken as the derivative of this. As seen from Figure 4.5, the maximum burn rate occurs approximately between

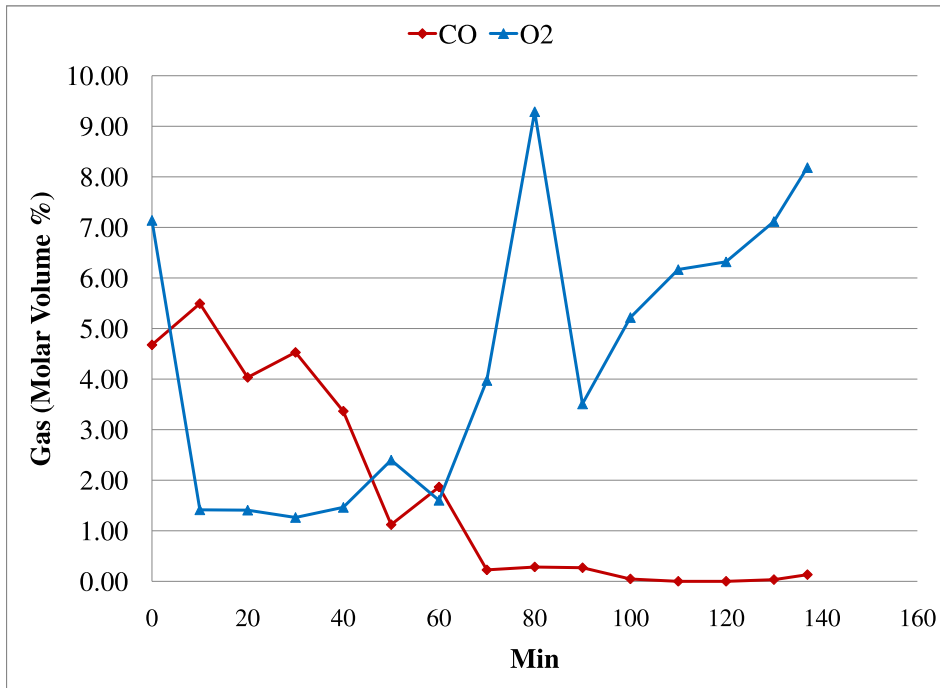


Figure 4.4: Gas mole fraction percentages from an EPA test Category 4 burn

the 40th and 60th minute.

#### 4.3.2 System Stoichiometry and Air-Fuel Ratio

With the burn rate known we can now use the dry gas meter data to investigate the stoichiometry of the burn. As discussed earlier, the wood proceeds through four stages of combustion and a plethora of surrogate fuels is suggested for such calculations. Here we investigate three in particular: formaldehyde as a surrogate for pyrolysis, carbon as a surrogate for char combustion, and the “wood molecule” derived from the ultimate analysis of white oak representing the entire combustion process. A liquid water fraction representing the moisture content of the wood is also included in the chemistry equation, however because the dry gas meter neglects the moisture content of the exhaust gas this quantity is not significant. The product species are limited to CO, CO<sub>2</sub>, H<sub>2</sub>O, O<sub>2</sub>, and

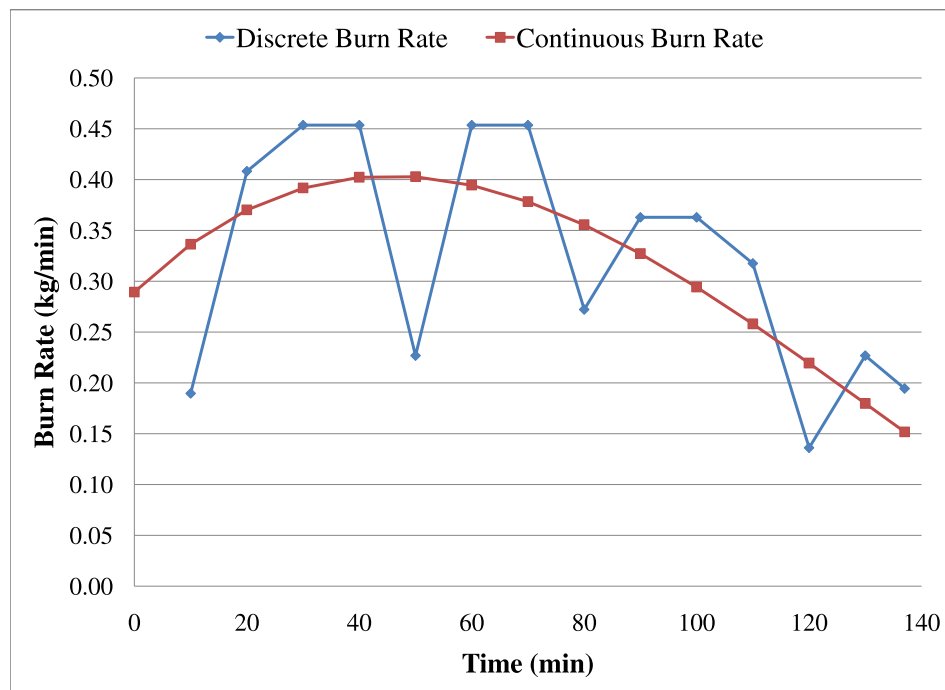


Figure 4.5: Category 4 discrete and continuous burn rate

$N_2$ . Unburned fuel and particulate are important from an environmental standpoint, but these are trace species that do not significantly affect the stoichiometry and thus can be ignored without significant error.

With the above mentioned assumptions, burn rate, and surrogate fuel molecules, we can determine the following information: the excess air coefficient  $\Theta$  defined by Equation A.1, the equivalence ratio  $\varphi$  defined by Equation A.9, and the stoichiometric air flow rate. Figure 4.6 shows the calculated values of  $\Theta$  and  $\varphi$  during a Category 4 burn. The mole fraction of CO during the run is also included to help understand the significance of  $\Theta$  and  $\varphi$ . First it should be noted that  $\varphi$  is simply a scalar multiple of  $\Theta$ ; second that with a surrogate fuel of  $CH_2O$ , once the CO concentration drops to zero,  $\varphi$  rises above one. This shows that  $\varphi$  indicates what we already know - that the combustion was incomplete because of the presence of CO. Unfortunately  $\Theta$ , which is always above one, also confirms

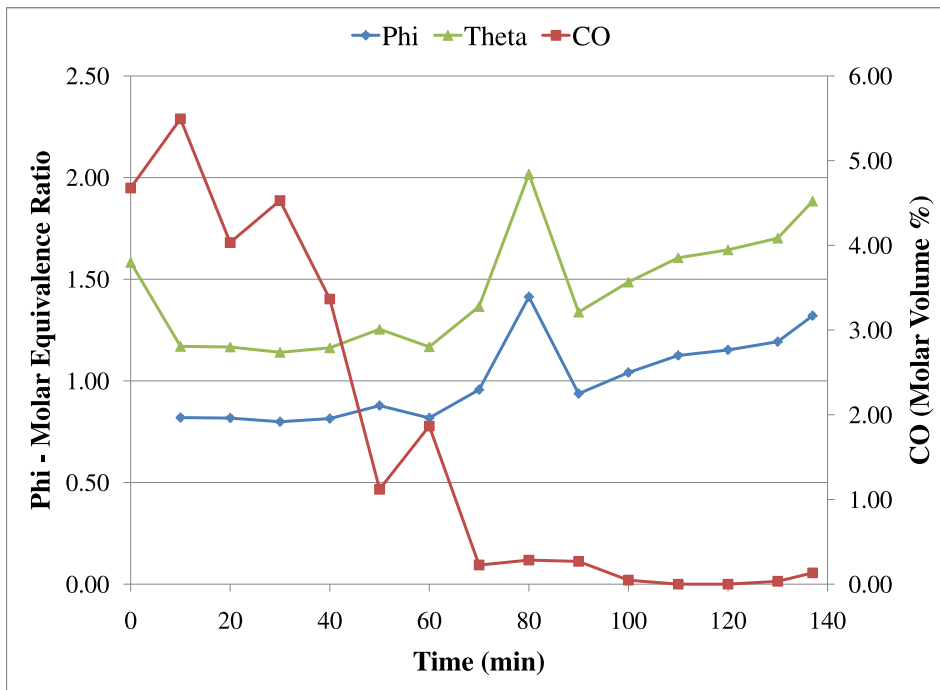


Figure 4.6: Excess air and equivalence ratio (surrogate fuel:  $\text{CH}_2\text{O}$ )

that there is excess air in the system. The small amount of CO produced must be from fuel lean combustion that is mixing limited, not from fuel rich combustion. This will be discussed again in Section 5.2.4.

Now we look at what the different fuel molecules tell us about the burn. In Figure 4.7 the stoichiometric air flow rate is plotted against the orifice measured air flow rate for all three fuel molecules. This comparison will hopefully show the applicability of each fuel molecule and serve as another verification of the total air flow to the furnace. From Figure 4.7a it is clear that the stoichiometric air flow rate matches best that measured by the orifice from about the 40th through the 80th minute. As specified earlier this is about the period of peak pyrolysis according to the burn rate. This indicates that this fuel molecule is best suited as a surrogate for this period of the burn. In a similar fashion it can be said that the flow rates for the “wood molecule” fuel match on average

throughout the burn and the carbon molecule only near the end, and therefore these fuels are best suited as approximates for the entire burn and the end of the burn respectively.

#### *4.3.3 Fire Brick and Water Jacket Temperatures*

To determine the fire brick temperature a basic heat transfer calculation was used. It included conduction from the inside to outside of the secondary chamber, convection from the combustion gasses, and radiation exchange between the gases and brick surface. The relevant geometries and directions of heat transfer are shown in Figure 4.8.

This led to the following equation for conservation of energy at the brick surface. From here the brick temperature could be found by iteration. A full explanation of the calculation is given in Appendix C.

$$q_c'' = q_{rad}'' + q_{conv}'' \quad (4.3)$$

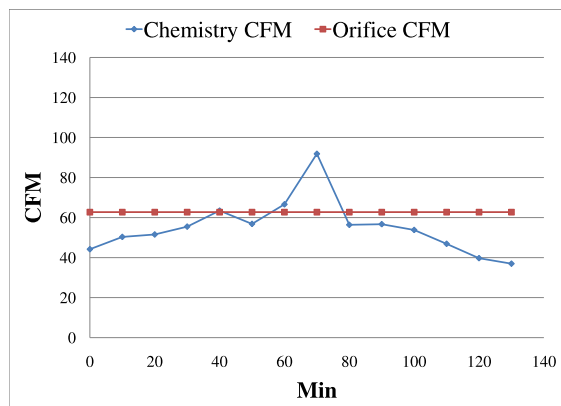
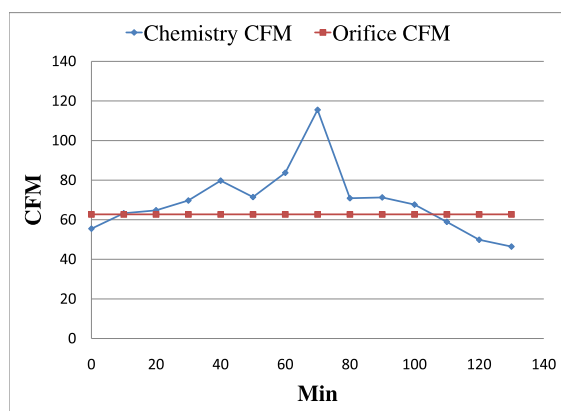
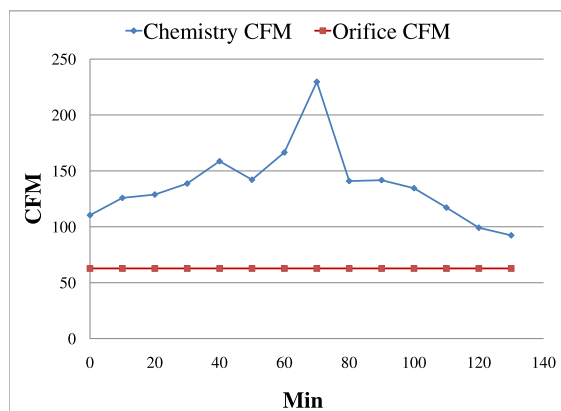
(a) CFM  $\text{CH}_2\text{O}$ (b) CFM  $\text{CHON}$ (c) CFM  $\text{C}$ 

Figure 4.7: Stoichiometric Airflow (CFM) for 3 different surrogate fuel molecules

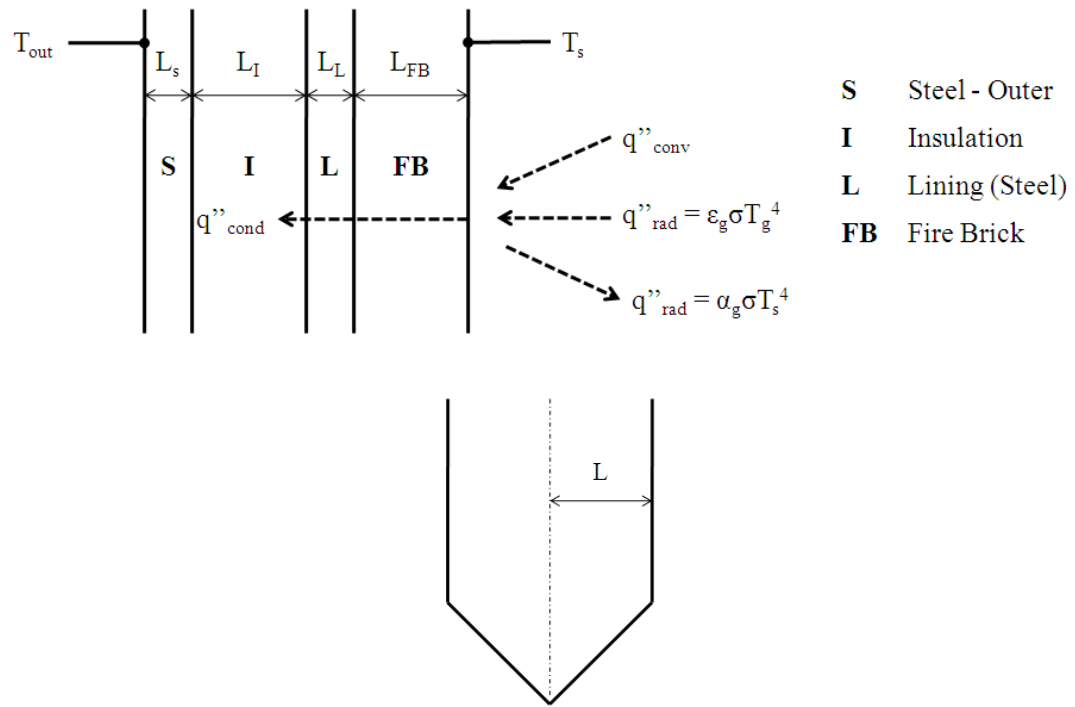


Figure 4.8: Description of heat transfer at the fire brick surface

## Chapter 5

### SLOTS STUDY

#### **5.1 Modeling Decisions and Initialization**

##### *5.1.1 The FLUENT CFD Software Package*

The CFD software FLUENT version 6.3 was used for the slots study. It is a widely used commercial code employing a finite volume discretization method to iteratively solve coupled differential equations particular to fluid flow studies. These include Navier-Stokes, conservation of energy, conservation of mixture fraction, various turbulence models, and species concentrations from various combustion models, as well as others. The following outline illustrates how the governing equations are solved in FLUENT [2]:

- Division of the domain into discrete control volumes using a computational grid.
- Integration of the governing equations on the individual control volumes to construct algebraic equations for the unknowns such as velocity, pressure, temperature, etc.
- Linearization of the discretized equations and solution of the resultant linear equation system to yield updated values of the dependent variables.

Readying a model for the FLUENT software is just as involved however. First, the computational domain is created via the accompanying software, GAMBIT. Here, boundary conditions are specified, fluid zones identified, and a mesh generated. This computational grid is then loaded into FLUENT; modeling decisions are made, equations chosen, and boundary conditions and parameters quantified. To solve the now well defined problem, a solution method is chosen and the solution initialized before iterations begin. Finally we look for convergence by monitoring the residuals.

The first ‘modeling decision’ involves the Navier-Stokes equations, for they take special care to solve. FLUENT allows us to choose one of two basic numerical solvers: the pressure based, or density based solver. Because of the low Mach number flows in the Aspen, the pressure based solver is chosen. This obtains the velocity field from the momentum equation and extracts the pressure field by solving a pressure or pressure correction equation which is obtained by manipulating the continuity and momentum equations [2]. This is referred to as pressure-velocity coupling, and the algorithm chosen for this study is the SIMPLE algorithm, or Semi-Implicit Method for Pressure Linked Equations.

The second ‘modeling decision’ requires choosing a discretization scheme. By default FLUENT stores discrete values of the ‘unknown’, call it  $\phi$ , at the cell centers. However, the face values  $\phi_f$  are required for the convection terms in the governing equations and must be interpolated from the cell center values. In this study, this is accomplished using an upwind scheme, where the face value  $\phi_f$  is derived from quantities in the cell upstream relative to the normal velocity  $v_n$  [2].

This applies to all unknowns except for the pressure. Because of the pressure-velocity coupling discussed above, a separate pressure interpolation scheme must be chosen, and thus we come to the third and final ‘modeling decision.’ For most cases the “standard” scheme is acceptable, but for flows with high-Rayleigh-number natural convection the PRESTO! scheme is suggested (PREssure STaggering Option). Since this study deals with a buoyant flame the PRESTO! scheme is chosen.

Finally, to prevent oscillatory behavior or divergence of the solution, under-relaxation factors (URFs) are used and changed as the iteration progresses. These values reduce the ‘step’ taken during iteration and therefore help to prevent overshooting in the solution. This is illustrated by Equation 5.1. Typical values for these URF’s are discussed during their usage in the problem setup.

$$\phi_{new} = \phi_{old} + (URF)\Delta\phi \quad (5.1)$$

### 5.1.2 Convergence and Accuracy

Numerical solutions of fluid flow and heat transfer problems are only approximate solutions. It is therefore very important to understand the shortcomings of the solutions obtained. This can be done by answering two questions: (1) has the solution converged? (2) how accurate is it?

In this study, convergence of iterative solutions is measured by residuals. These can be thought of as the remainder for each equation summed over the computational domain. In general however, it is difficult to judge convergence by examining the magnitude of this value alone, rather a “scaled” residual is employed. The pressure-based solver’s scaled residual for the continuity equation is defined as the unscaled residual divided by the largest absolute value of the continuity residual in the first five iterations. The common limits of convergence for the scaled residuals is  $10^{-3}$  for all equations except energy, mixture fraction, and radiation for which the criterion is  $10^{-6}$  [2].

Once a solution is obtained we must address its accuracy. There are many possible sources of error and these are summarized and grouped into three categories by Ferziger [9]:

1. *Modeling Errors*, which are defined as the difference between the actual flow and the exact solution of the mathematical model. Modeling approximations such as fuel choice, steady state assumptions (etc) play a large role in this. Issues regarding modeling errors for the Slots Study is discussed later in this chapter.
2. *Discretization Errors*, also known as grid dependency, are defined as the difference between exact and discretized numerical solutions. The effects of grid refinement on the solution is addressed in this study.
3. *Iteration Errors*, are defined as the difference between the iterative and exact solutions of the algebraic system of equations. The convergence criteria outlined above serve to minimize this error.

Numerical diffusion, which falls under “Discretization Errors” is a dominant source of

error in multidimensional problems and is particularly relevant to this study. It is most noticeable at low Reynolds numbers when the convective contribution is small. Numerical diffusion arises both from truncation errors in the discretization of the equations and from the chosen interpolation method ('upwind' in Fluent's case). Therefore, all practical numerical schemes for solving fluid flow problems result in some numerical diffusion, but its effects can be mitigated. The first approach is to refine the grid because the amount of numerical diffusion is inversely proportional to the resolution of the mesh. It should also be noted that 'false diffusion' is also minimized when the flow is aligned with the grid. Generally speaking, for tetrahedral grids the flow is never aligned, however for a complex flow the odds of alignment do not improve by using a structured quadrilateral/hexahedral mesh [2]. The second approach is to increase the order of discretization, and in FLUENT we can choose from either a first or second order scheme. Because an unstructured, tetrahedral mesh is used for this study, the second-order scheme is chosen.

### *5.1.3 Grid Development*

The computational domain was created in the pre-processing software, GAMBIT, and is based on the manufacturer's drawings to ensure agreement with the existing furnace. We are interested in characterizing the combustion through the slots and have a limited amount computational memory; we therefore omit the fire tube heat exchanger and exit stack, adding a superficial exit instead.

Meshing the domain proved problematic because of the differences in scales between the large volume of the combustion chambers and the very slender slots - the primary chamber's width is 60 cm while a slot's width is only 2 cm. Rapid changes in cell volume between adjacent cells is not recommended because it leads to large truncation errors (the difference between the partial derivatives in the governing equations and their discrete approximations) [2]. Therefore when we refine the grid through the slots, we must refine the grid throughout the domain. This significantly increases computational costs. The optimal mesh density had to be determined during the combustion runs. The

metric chosen for determining grid independence of the solution was the mass weighted average, CO mole fraction at the top (upstream) and bottom (downstream) of the slots. Due to the complexity of the geometry and the inability to anticipate the direction of cell normal velocities, an unstructured mesh of tetrahedral cells was used for all runs.

Table 5.1: Summary of computational grids

Grid Number	Grid Size (# of elements)
Grid 1	4,763,875
Grid 2	5,409,456
Grid 3	5,615,316

#### 5.1.4 Modeling Decisions

Many of these modeling decisions are directly derived from the discussion of ‘Fundamental Concepts.’ First, the flow field is modeled using the Realizable  $k - \varepsilon$  turbulence model. This is chosen over the RNG and Standard models because of runaway turbulent viscosity ratios in primary chamber recirculation areas and the Realizable model’s superior performance in such flow regions. Also, ‘full buoyancy effects’ is included to account for buoyancy in the  $\varepsilon$  equation.

The surrogate pyrolysis fuel was chosen to be Huttenen’s Composition 2. Glanville made use of several surrogate fuel compositions including both of Huttenen’s suggestions, and formaldehyde with Bhaskar’s enthalpy of formation, and found that Composition 2 produced exhaust CO concentrations much closer to measured values for the updraft combustor. Huttenen’s approximated fuel compositions are provided in Table 5.2.

Based on this chosen fuel a lookup table was calculated. The stoichiometric value of mean mixture fraction at a heat flux of zero was found to be  $Z = 0.172$ . The resulting look

Table 5.2: Estimates for the composition of the pyrolysed fuel [13]

Species	Mole Fraction	
	Composition 1 (%)	Composition 2 (%)
CO <sub>2</sub>	14.6	9.6
CO	33.3	38.3
CH <sub>4</sub>	20.8	23.9
H <sub>2</sub> O	2.1	10.0
H <sub>2</sub>	29.2	18.2

up table for density, temperature and species mass fraction, calculated using equilibrium chemistry and a  $\beta$ -distribution assumed-shape PDF, is shown in Figure 5.1.

Finally, radiation exchange is accounted for with the Discrete Ordinance Model (DO). To include absorption by product gases, notably CO<sub>2</sub> and H<sub>2</sub>O, the weighted-sum-of-gray-gasses model (WSGGM) was used to calculate the gas absorption coefficient [2].

### 5.1.5 Boundary Conditions

The Slots Study is conducted as a snapshot of the furnace operation during peak pyrolysis, therefore all boundary conditions are set as averages of test data from the 40th to 60th minute of combustion.

#### *Air Inlet*

When the air path is included in the domain, a single air inlet face is used. This is set as a mass flow rate of 0.036288 kg/s, entering at atmospheric pressure and 300 K. Turbulence parameters are calculated as shown in Appendix C.

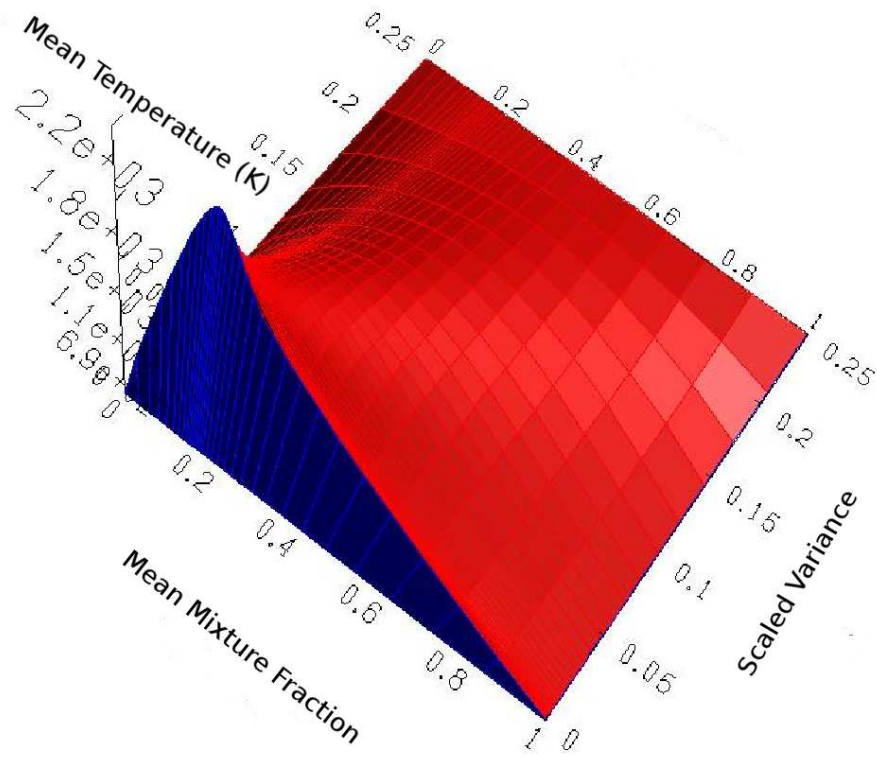


Figure 5.1: PDF look up table

### *Fuel Inlet*

A fluid volume set 0.75 inches from the crib wood surfaces is separated from the primary combustion chamber, and the fuel is introduced here as the volumetric source term of  $0.16303 \text{ kg/s-m}^3$ , corresponding to the peak burn rate (peak pyrolysis). This is chosen rather than introducing the fuel at the crib wood surface to prevent solution instabilities and overestimation of fuel transport [11].

### *Internal Surfaces*

The internal surface temperatures are determined via combustion test data and previous analyses. The temperature of all secondary chamber fire-brick is approximated as 1296 K, which was found in section 4.3.3 to be the temperature of the fire brick wall of the secondary chamber. Using a simple conduction analysis the temperature of the primary chamber fire-brick was determined to be 1201 K. The steel water jacket temperature is approximated as 331 K, which is the measured temperature of the water. This is reasonable because of the high thermal conductivity of steel. Finally the wood surface temperature is assumed to be 573K, which is the observed solid phase pyrolysis temperature [13]. Since radiation is also included, an emissivity for each surface must be specified. All surfaces are approximated as blackbodies; the steel is painted black, the surface of the pyrolysed wood is actually char, and fire clay has an emissivity close to one. Therefore all emissivities were approximated as one.

#### *5.1.6 Simulation Strategy*

While each simulation has unique iterative behavior, a general simulation strategy is employed to give cohesiveness to the solutions. First, the simulation is always initialized from the air inlet, providing the first solution guess. Some suggest that a cold flow solution be converged first and this used as the initial guess for the combusting run. Unfortunately the cold flow solution appeared to be a poor initial guess, had little impact on our final solution, but did increase computation time. For these reasons a cold flow

solution was not used to initialize a combusting run. To prevent oscillations during ignition, iterations were damped through the use of reduced under-relaxation factors (URFs) for density, momentum, and energy. This is run for 300-400 iterations to establish the flow. Then, to assure accurate chemistry modeling and convective species transport the pressure and mean mixture fraction URFs are increased and the momentum URF reduced and the simulation run to convergence.

## **5.2 Results and Discussion**

Results from the Slots Study simulations are compared across three grid resolutions and two air flow scenarios. The scenarios are then compared with the following measured quantities: air flow rates for each port, and CO<sub>2</sub>, CO, and O<sub>2</sub> stack dry gas concentrations. Again, we are most interested in determining how the CO concentration evolves through the slots, and whether or not the secondary air has a significant affect on this result. We also note that the flow in Slot 4 has a significant CO concentration, therefore many of the following comparisons are made using this slot as an example.

### *5.2.1 Quantifying Grid Independence*

The number of computational cells ranges from 4.7 to 5.6 million, with exact values given in Table 5.1. The varied grid densities were used to estimate the grid dependence of the solution field. This was evaluated qualitatively with the appearance of the flame structure in the primary chamber, and the velocity profile through the slots; as well as quantitatively with CO concentrations at the top and bottom of the slots, and the change in CO concentration across the slot.

Looking at the furnace as a whole, we see that the flame structure in the primary chamber changes significantly with grid density (Figures 5.2a, 5.2b, and 5.2c). This can most likely be attributed to numerical diffusion amplified by low Reynolds numbers near the fuel inlet (Figure 5.3). This results in artificial flame spreading, and the larger more robust looking flame in the lower resolution grid of Figure 5.2a. The FLUENT manual

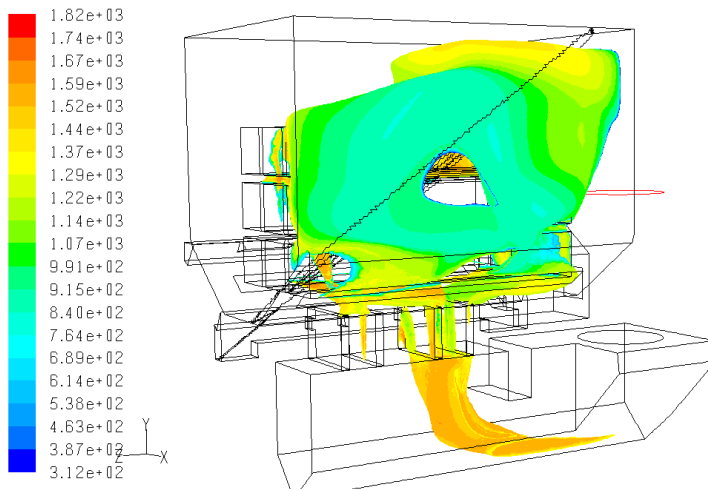
also suggests that due to the strong interaction of mean flow and turbulence, numerical results for turbulent models are more susceptible to grid dependence than those for laminar flows [2]. This may be especially true for the Realizable turbulence model which uses the mean flow and turbulence to determine  $C_\mu$  in the turbulent viscosity equation, rather than using a set constant.

Because of the significant influence of the flow field on reaction progression, we verified that the grid resolutions were sufficiently refined for adequate velocity field development in the slots. Again, Slot 4 is used as an example and the contours of velocity magnitude are plotted in Figures 5.4a, 5.4b, and 5.4c.

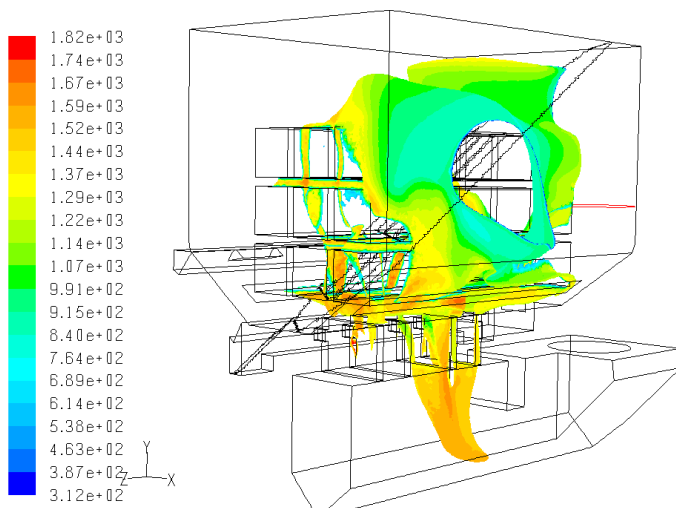
We are not interested in modeling the full behavior of the furnace, so the apparent grid dependence only concerns us if it affects the values of interest. Table 5.3 gives a comparison of the evolution of CO mole fraction through each slot for each of the three grid resolutions. Taking Slot 4 as an example, the CO mole fraction at the top of the slot varies from 6.77% to 4.30% for Grids 1 and 3 respectively, a difference of 2.5% and a change of almost 36%. The difference between Grid 2 and Grid 3 however is only a few tenths of a percent.

Table 5.3: Comparison of CO mole fractions at the top and bottom of each slot for three grid resolutions

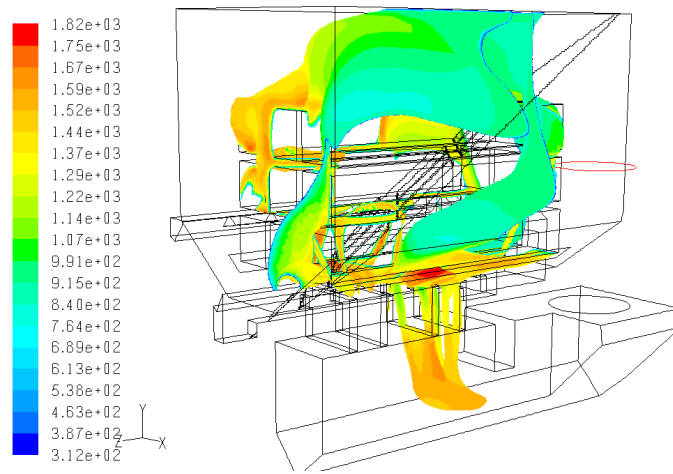
		Slot Number				
	Grid Number	1	2	3	4	Average
Top (mole fraction %)	Grid 1	0.09	0.96	6.63	6.77	<b>3.65</b>
	Grid 2	0.32	0.98	5.09	4.90	<b>2.91</b>
	Grid 3	0.49	0.89	5.30	4.30	<b>2.85</b>
Bottom (mole fraction %)	Grid 1	0.00	0.11	5.48	6.07	<b>2.97</b>
	Grid 2	0.00	0.02	4.46	4.27	<b>2.29</b>
	Grid 3	0.00	0.00	4.76	3.50	<b>2.18</b>



(a) Grid 1



(b) Grid 2



(c) Grid 3

Figure 5.2: Flame Structure - Contours of temperature on  $Z_{stoich}$  iso-surface

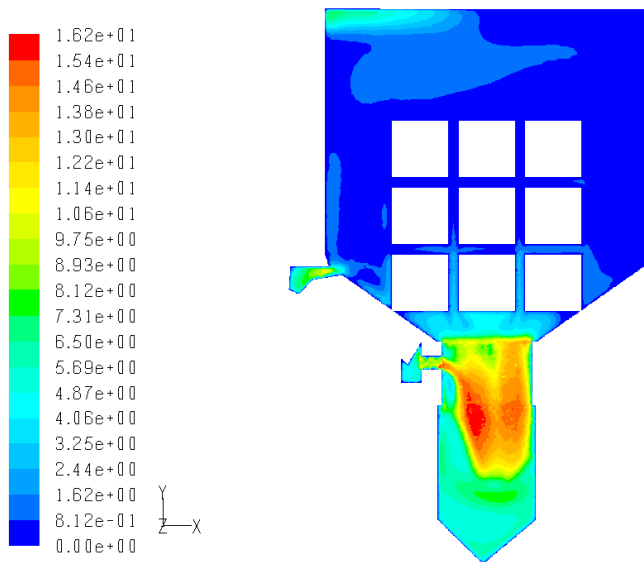
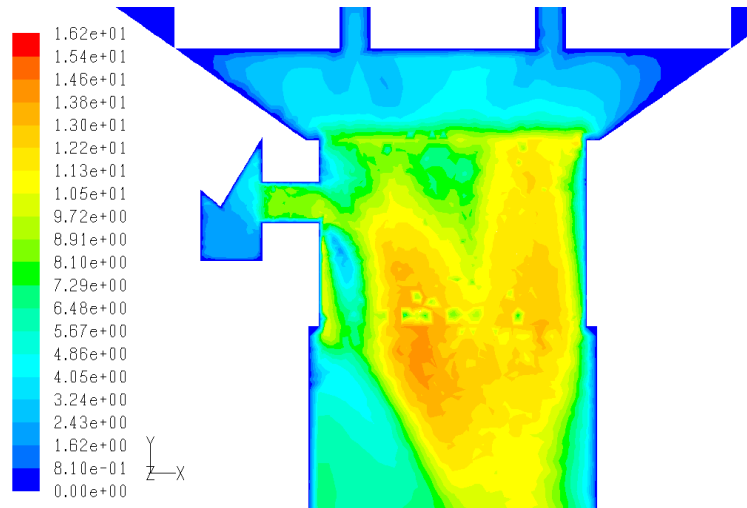


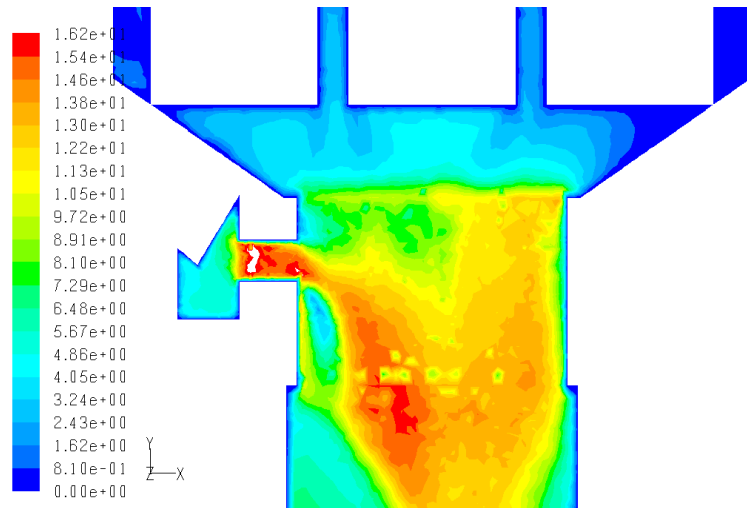
Figure 5.3: Velocities on a plane through Slot 4 for Grid 3

The other issue at hand is whether or not, the behavior of CO concentration through the slots remains consistent for each of the grid resolutions. We therefore examine the change in CO concentration through the slots for each grid density (Table 5.4). Results from Grids 2 and 3 are relatively consistent.

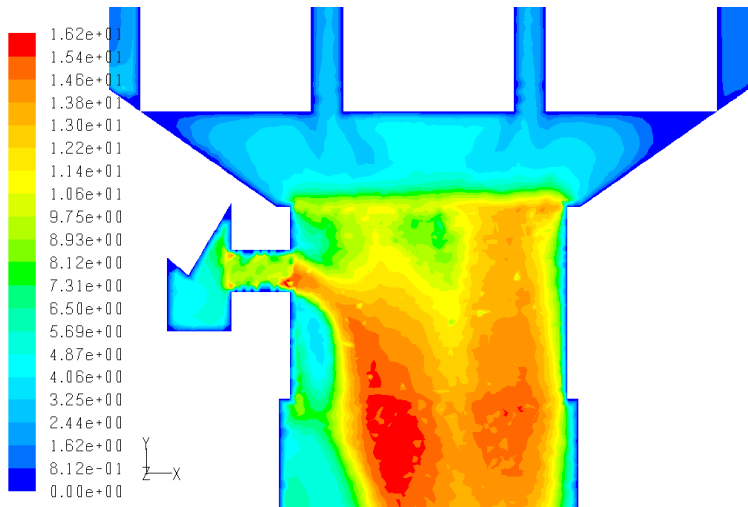
Both qualitative and quantitative evidence points to some grid dependence for the values of interest, and unfortunately further grid studies could not be performed because of a lack of computational power and time (Grid 3 required over 6GB of memory and required up to 24 hours of computation time). The differences across quantitative data taken from Grids 2 and 3 however is relatively small, and the CO concentration trend through the slots is maintained. It is therefore assumed that Grid 3 closely approaches the final grid independent solution and it is the grid chosen for subsequent models.



(a) Grid 1



(b) Grid 2



(c) Grid 3

Figure 5.4: Contours of velocity through Slot 4

Table 5.4: Comparison across three grids of the change in CO concentration through the slots

		Slot Number				
	Grid Number	1	2	3	4	<b>Average</b>
Change (mole fraction %)	Grid 1	0.09	0.85	1.15	0.70	<b>0.69</b>
	Grid 2	0.32	0.96	0.63	0.63	<b>0.62</b>
	Grid 3	0.49	0.89	0.53	0.81	<b>0.67</b>

### 5.2.2 Air Distribution

Two scenarios are run on Grid 3: (1) with secondary air (2) without secondary air. These are each run in a cold air flow only and full burn simulation, the results of which are given in Table 5.5. The air flow measurements could only be taken under cold flow conditions, but FLUENT allows us to investigate how the distribution changes when the furnace is in operation and the air density drops.

Table 5.5: Comparison of measured and calculated air flow rates for each air port, reported as percentages of the total air flow rate

		Secondary				Side		Top
	Port Number	1	2	3	4	1	2	-
	<b>Measurements</b>	<b>0.8%</b>	<b>0.8%</b>	<b>0.8%</b>	<b>0.8%</b>	<b>12.0%</b>	<b>28.0%</b>	<b>57.0%</b>
With Secondary Air	FLUENT - Cold	4.2%	4.1%	4.1%	4.0%	25.4%	11.7%	46.7%
	FLUENT - Burn	3.5%	3.4%	3.9%	4.0%	20.0%	15.2%	50.0%
Without Secondary Air	FLUENT - Cold			-		31.1%	13.8%	55.1%
	FLUENT - Burn			-		24.0%	17.7%	58.3%

FLUENT significantly over predicts secondary air flow to the slots. In the actual furnace system the air must travel through irregularly shaped passageways, over rough ceramic fire brick and loose mineral fiber insulation blankets. The significant difference

Table 5.6: Hand calculation of air split as a function of constriction to secondary air passage

Constriction	Secondary	Side	Top
none (8 cm <sup>2</sup> )	50%	35%	15%
75% (2 cm <sup>2</sup> )	57%	38%	4%

between the measured and simulated air flow rates is likely due to an under estimation of the pressure losses in the passageways. There is a significant constriction in the passageway leading to the secondary ports, about 8 cm<sup>2</sup> in area. (For comparison, the smallest constrictions leading to the Top and Side Ports are about 30 cm<sup>2</sup> in area). This small area can very easily be blocked by the insulation.

The effect of a blockage in this passageway can be roughly approximated with a simplified hand calculation. The passageways are modeled as three parallel pipes connecting two large reservoirs. Minor losses include 90° elbows and area expansions. Individual exit nozzles are not modeled, but rather the areas of the exits (e.g. Side Ports 1 and 2 of the Slots passageway) are added together and counted as a single exit with the associated loss modeled as an area expansion. The baseline hand calculation for cold flow provides remarkably good agreement with FLUENT’s solution. The spreadsheet solution is given in Appendix B. Using this hand calculation we are able to estimate the necessary constriction in the secondary air passage for agreement between the measured and calculated air flow rates. The results are given in Table 5.6.

FLUENT also reverses the air flow rates through the Side Ports. Normally we would expect the flow rate through the port furthest from the air inlet (Side Port 2) to have a smaller flow rate than those that are closer because of the static pressure drop along the passageway. In a burn run for scenario 1, however, just before Side Port 2 FLUENT gives the static pressure in the air passageway to be between -54 and -56 Pa and just after the port to be between -46 and -45 Pa. The classic pipe equation (modified Bernoulli)

given by Equation 5.2 reveals why this occurs. Velocity B, downstream of Side Port 2 is significantly less than velocity A upstream of Side Port 2, and if the head loss predicted by the friction factor is not large enough to make up the difference, pressure B must increase to maintain the equality. In the HVAC industry this is known as static regain, and accounts for the higher flow rate in the port furthest from the inlet predicted by FLUENT. In the actual furnace if the friction factor is much greater than that used in the FLUENT model, then pressure B will indeed drop and the flow rate for Side Port 2 will be less than that for 1.

$$P_A + \rho \frac{V_A^2}{2} = P_B + \rho \frac{V_B^2}{2} + f \frac{l}{D} \frac{\rho V^2}{2} \quad (5.2)$$

We take the two simulation scenarios as bounds on the ability of the furnace design to deliver secondary air. The cold flow simulation of Scenario 2 without secondary air produces good agreement with the air flow rate in the top port, and therefore total flow through the Side Ports. Although the flow rates through the Side Ports are significantly different from measured values, we do not include a scenario in which we artificially specify the air distribution for two reasons: (1) the air flow distribution changes during a burn and we were not able to measure the distribution during a burn (2) we are not interested in the behavior of the flame in the primary chamber and don't believe the change in Side Port flow rates would significantly affect our evaluation of the slot performance.

### 5.2.3 Furnace Emissions

A comparison of stack species concentrations from both simulation scenarios and EPA test data highlights the short comings of the simulations in predicting full furnace performance. The comparison was made for the same 'snapshot' in time (40th to the 60th minute), and the concentrations from the simulations were taken at the outlet of the secondary burn chamber. It was assumed that once the exhaust gasses entered the fire tubes of the heat exchanger, all reactions would be quenched. Figure 5.5, shows that the

simulations under predict  $\text{CO}_2$  and most importantly  $\text{CO}$  concentrations, but over predict  $\text{O}_2$  concentrations. This could be the result of an inaccurate modeling assumption: the air flow rate may have been too large, the fuel burn rate too small, or the carbon content of the fuel approximation too low. Altering one of these modeling approximations may have resulted in a larger  $\text{CO}_2$  concentration, closer to test measurements, but it would not have necessarily improved the  $\text{CO}$  concentration agreement.

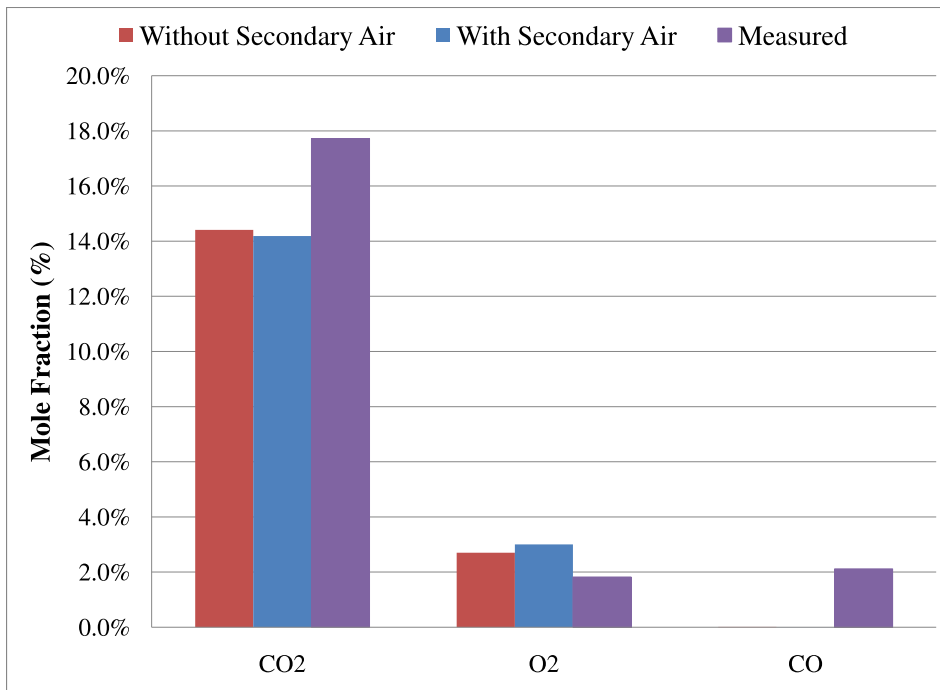


Figure 5.5: Stack species concentrations of test data vs. simulations

#### 5.2.4 Slots

We now investigate how the different air distributions discovered above affect the  $\text{CO}$  concentration through the slots, and contribute to the overall emissions performance of the furnace. Plots of  $\text{CO}$  mole fraction contours for both scenarios are shown below. When secondary air is included, pathlines from the secondary air inlet are given to show

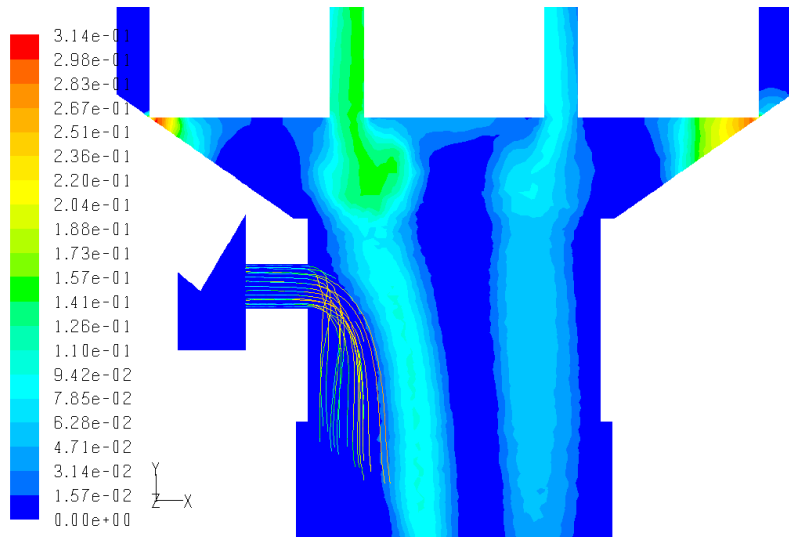
jet penetration (Figure 5.6).

Generally speaking, secondary air is introduced in jets, not only to bring air levels up to or past the stoichiometric level but also to induce mixing. The mixing helps to ensure that the excess air can reach the pockets of unburnt fuel, but requires significant penetration of the air jet. If the secondary air simply ‘trickles down’ the side of the slot, it contributes little to the completion of combustion. Figure 5.6a indicates the jet penetration is about 25% of the width of the slot.

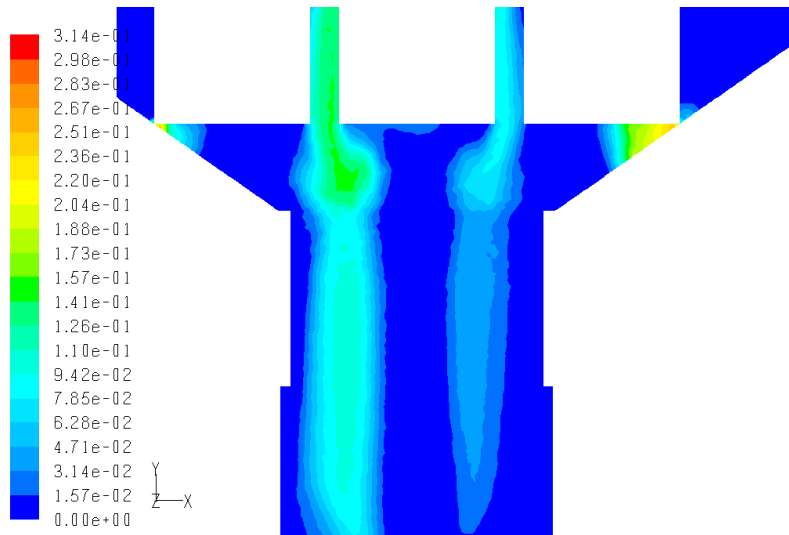
Qualitatively, the CO concentration in the slots appears to be similar for the two scenarios and the secondary air jet does appear to assist in reducing CO emissions. Table 5.7 reveals the quantitative comparison of slot performance for the two scenarios. In the scenario with secondary air, the primary chamber runs sub-stoichiometric with less of the CO oxidized before the slots. FLUENT therefore predicts higher CO concentrations at the top of the slots. The addition of secondary air then allows for further combustion and a drop of 0.5 to 0.9% in CO concentration through the slots. In running the primary chamber with excess air in Scenario 2, FLUENT predicts a lower concentration of CO at the top of the slots and a smaller drop through the slots (0.2 to 0.4%). The final result however is that both scenarios have similar CO concentrations at the bottom of the slots, with that for Scenario 2 being only slightly lower than Scenario 1.

As we can see by comparing Figures 5.7 and 5.2c, CO persists further downstream in Scenario 2 when no secondary air is added. So while the CO concentration at the bottom of the slots is lower under Scenario 2, the oxidation of the CO in the secondary chamber is slower, and therefore the probability of it reaching the stack, greater.

Based on the change in CO concentration through the slots we can say that the slots by themselves do improve combustion efficiency. The addition of secondary air appears to have more of an affect on combustion efficiency in the secondary chamber than in the slots.



(a) Scenario 1 - with secondary air pathlines



(b) Scenario 2

Figure 5.6: Contours of CO mole fraction and the influence of secondary air

Table 5.7: Comparison between simulation scenarios of CO mole fractions behavior in the slots

	Scenario	Slot Number				Average
		1	2	3	4	
Top (mole fraction %)	With Secondary Air (1)	0.49	0.89	5.30	4.30	<b>2.85</b>
	Without Secondary Air (2)	0.32	0.43	4.33	3.61	<b>2.20</b>
Bottom (mole fraction %)	With Secondary Air (1)	0.00	0.00	4.76	3.50	<b>2.18</b>
	Without Secondary Air (2)	0.00	0.00	4.12	3.35	<b>1.90</b>
Change Through Slots	With Secondary Air (1)	0.49	0.89	0.53	0.81	<b>0.67</b>
	Without Secondary Air (2)	0.31	0.43	0.21	0.26	<b>0.30</b>

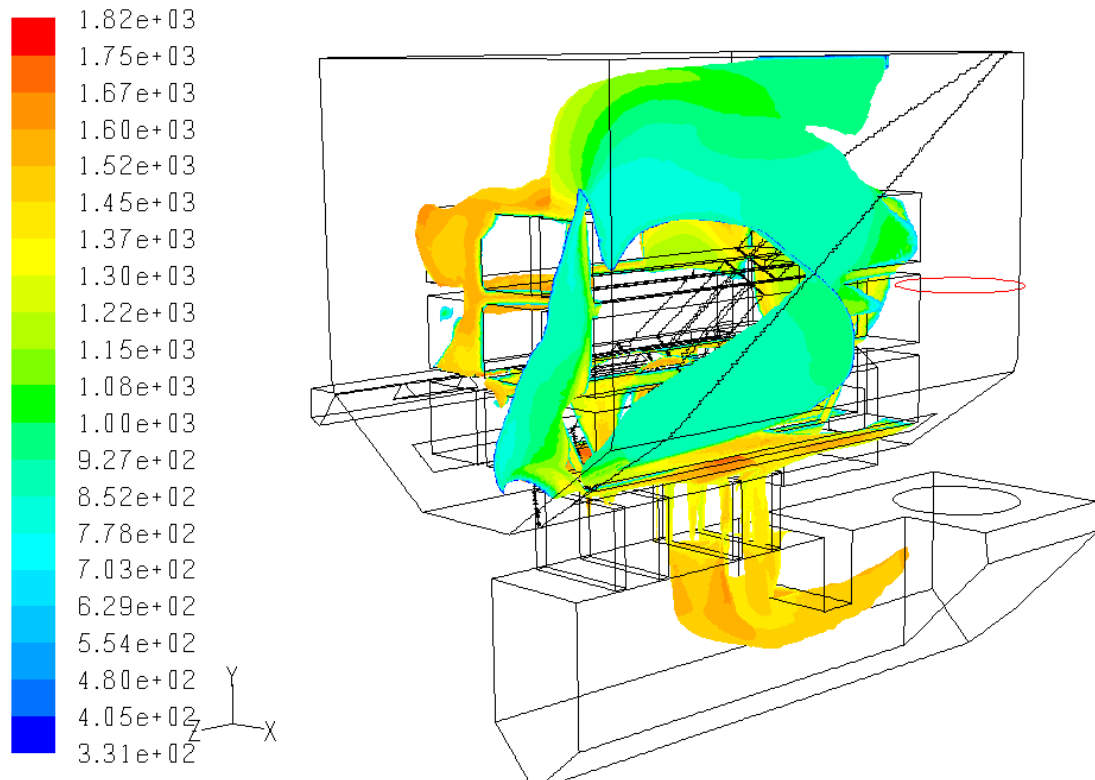


Figure 5.7: Flame Structure - Contours of temperature on  $Z_{stoich}$  iso-surface for scenario 2 without secondary air

## Chapter 6

### CONCLUSIONS AND RECOMMENDATIONS

A CFD study was carried out to examine the performance of the slots and secondary air addition in contributing to the reduction of PM emissions in the operation of a downdraft furnace. The study focused on a time ‘snap-shot’ where pyrolysis was at its peak, and oxidation of CO was used as the metric for combustion efficiency. By benchmarking the current operation of the furnace, and comparing this with results from the CFD simulations, we hoped to determine the necessity of secondary air in maintaining current particulate emission levels.

From the results presented, the following conclusions are drawn:

1. CO and therefore PM emissions are due to mixing limited combustion.
2. The slots by themselves do contribute to CO oxidation, and therefore total combustion efficiency and PM reduction.
3. The current furnace operates closer to the conditions of Scenario 2 with no secondary air addition.
4. In light of items 2 and 3, an EPA test of the Aspen under strict Scenario 2 conditions (no secondary air), is recommended as a viable method to determine if the slots are needed to achieve high CO burnout performance. If they are not needed, their elimination will substantially reduce the manufacturing costs of the unit.
5. Because of the grid dependence of the solution, which was especially evident in the primary chamber, the simulations cannot be considered reliable predictors of full furnace performance during peak pyrolysis.

Future work might focus on gaining a better understanding of the role secondary air injection has on mixing in the slots. This could be accomplished by using an inert gas instead of a combusting run. With the gas at the top of the slots and in the secondary air inlet having the same mixture fraction value, variance of mixture fraction could be used to measure the quality of mixing. This would help to quantify the amount of secondary air necessary for significant emissions improvement and optimize the dimensions of the slots towards the same end.

Further investigation into full furnace modeling should also be conducted. It is assumed that the turbulence modeling is the main reason for disagreement between predicted and measured stack CO concentrations. The next step in turbulence modeling would be a Large Eddy Simulation (LES). Although this would be a transient simulation and more computationally expensive, it may better capture the large turbulent eddies that are most likely responsible for the CO stack emissions.

## BIBLIOGRAPHY

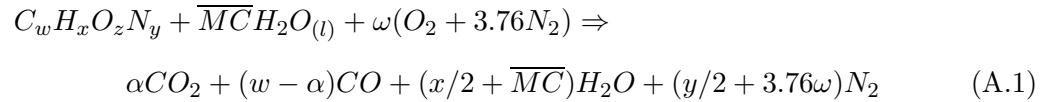
- [1] The off grid home. <http://theoffgridhome.com/2008/03/18/87/>.
- [2] *FLUENT 6.3 User's Guide*, 2006.
- [3] M.O. Andreae and G. Gelencser. Black carbon or brown carbon? the nature of light-absorbing carbonaceous aerosols. *Atmospheric Chemistry & Physics*, 6:3131–3148, 2006.
- [4] X.S. Bai, N. Griselin, T. Klason, and J. Nilsson. Cfd modeling of biomass combustion in small-scale boilers - final report. Technical report, Division of Fluid Mechanics, Department of Heat and Power Engineering, Lund Institute of Technology, Lund, Sweden, 2002.
- [5] S. Choi and D. Shin. The combustion of simulated waste particles in a fixed bed. *Combustion and Flame*, 121:167–180, 2000.
- [6] G. Cox, editor. *Combustion Fundamentals of Fire*. Academic Press, 1995.
- [7] C. Di Blasi. Modeling and simulation of combustion processes of charring and non-charring solid fuels. *Prog. Energy Combust. Sci.*, 19:71–104, 1993.
- [8] C.S. Bhaskar Dixit, P.J. Paul, and H.S. Mukunda. Part ii: Computational studies on a pulverised fuel stove. *Biomass and Bioenergy*, 30:684–691, 2006.
- [9] J.H. Ferziger and M. Peric. *Computational Methods for Fluid Dynamics*. Springer, third edition, 2002.
- [10] P. M. Fine, G. R. Cass, and B. R. Simoneit. Chemical characterization of fine particulate emissions for fireplace combustion of woods grown in the northeastern united states. *Environmental Science and Technology*, 35:2665–2675, 2001.
- [11] P. Glanville. Reducing particulate matter emissions from a wood-fired hydronic furnace: computational fluid dynamics modeling and analysis. Master's thesis, University of Washington, 2008.

- [12] M.L. Hobbs, P.T. Radulovic, and L.D. Smoot. Combustion and gasification of coals in fixed beds. *Prog. Energy Combust. Sci.*, 19:505–586, 1993.
- [13] M. Huttenen, J. Saastamoinen, and et.al. Emission formation during wood log combustion in fireplaces - part i: volatile combustion stage. *Progress in Computational Fluid Dynamics*, 6(4/5):200–208, 2006.
- [14] F. Incropera and D. Dewitt. *Introduction to Heat Transfer*. John Wiley & Sons, fourth edition, 2002.
- [15] James E. McCarthy. Clean air act: A summary of the act and its major requirements. Technical report, CRS Report for Congress, 2005.
- [16] D. Munson, B. Young and T. Okiishi. *Fundamentals of Fluid Mechanics*. John Wiley & Sons, fifth edition, 2006.
- [17] Department of Energy. Residential energy consumption survey, 2001.
- [18] B. Peters. *Thermal Conversion of Solid Fuels*. WIT Press, 2003.
- [19] N. Peters. *Turbulent Combustion*. Cambridge University Press, 2000.
- [20] H. Thunman and B. Leckner. Co-current and counter-current fixed bed combustion of biofuel - a comparison. *Fuel*, 82(3):275–283, 2002.
- [21] D. Tillman, A. Rossie, and W. Kitto. *Wood Combustion: Principles, Processes, and Economics*. Academic Press, 1981.
- [22] S. Turns. *An Introduction to Combustion*. McGraw-Hill, Inc, 1996.
- [23] U.S. Environmental Protection Agency. *Method 5G: Determination of Particulate Matter Emissions from Wood Heaters (Dilution Tunnel Sampling Location)*.
- [24] U.S. Environmental Protection Agency. *Test Method 28: Measurement of Particulate Emissions and Heating Efficiency of Outdoor Wood-Fired Hydronic Heating Appliances*.
- [25] Y.B. Yang. Numerical simulation of the burning characteristics of thermally-thick biomass fuels in packed-beds. *Process Safety and Environmental Protection: Transaction of the Institute of Chemical Engineers, Part B.*, 83(6), 2005.

## Appendix A

**GENERAL FUEL CHEMISTRY**

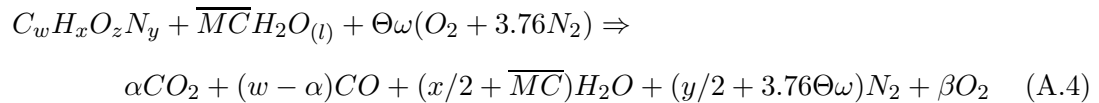
Goal: Determine the total air flow rate to the furnace based on a generic fuel composition.

General Stoichiometric Reaction with COStoichiometric air with CO

$$\omega = \frac{1}{2}(\alpha + w + x/2 - z) \quad (\text{A.2})$$

Stoichiometric air without CO

$$\omega^* = \frac{1}{2}(2w + x/2 - z) \quad (\text{A.3})$$

General Excess Air Reaction with COSolving for  $\beta$ 

$$\beta = \frac{1}{2}(\Theta - 1)(\alpha + w + x/2 - z) \quad (\text{A.5})$$

Dry Exhaust Gas Mole Concentrations

$$y_{CO_2} = \frac{\alpha}{w + y/2 + 1/2(4.76\Theta - 1)(\alpha + w + x/2 - z)} \quad (\text{A.6})$$

$$y_{CO} = \frac{w - \alpha}{w + y/2 + 1/2(4.76\Theta - 1)(\alpha + w + x/2 - z)} \quad (\text{A.7})$$

solving for  $\alpha$ .

$$\alpha = \frac{y_{CO_2}(w + y/2 + 0.5(4.76\Theta - 1)(w + x/2 - z))}{1 - 0.5y_{CO_2}(4.76\Theta - 1)}$$

$$\alpha = \frac{w - y_{CO}(w + y/2 + 0.5(4.76\Theta - 1)(w + x/2 - z))}{1 + 0.5y_{CO}(4.76\Theta - 1)} \quad (\text{A.8})$$

The dry gas mole fractions of  $CO$  and  $CO_2$  measured during a combustion run can now be used to calculate  $\Theta$ . The molar equivalence ratio, representative of true stoichiometric conditions without  $CO$  is defined as:

$$\varphi = \frac{\Theta\omega}{\omega^*} \quad (\text{A.9})$$

## Appendix B

**ORIFICE CALIBRATION AND BENCHMARKING**

Goal: Determine the discharge coefficient for the orifice being used

Equipment

Item	Accuracy	Comments and Sources of Error
Squirrel Cage Fan	-	turbulent flow caused variations in digital manometer reading
Duct	-	6in diameter, not quite round
Orifice	-	3in diameter, must be parallel to streamlines during measurement
Pressure Taps and Manometer	$\pm 0.03$	
Pitot Tube	-	
Digital Manometer		measures static pressure at pitot tube
Scale	$\pm 0.1mm$	-

Measuring Velocities

The pitot tube is used to measure fluid speed. The pressure measured at the pitot tube's tip is the stagnation pressure and this is related to the upstream velocity through the Bernoulli equation

$$P_n = P_{static} + 1/2\rho V^2 \quad (\text{B.1})$$

where  $P_n$  is the stagnation pressure at the point of interest,  $P_{static} \approx P_{atm}$  which is

atmospheric pressure, and  $\rho$  is the density of air.

### Velocity Profile and Volumetric Flow Rate

A velocity profile was measured across the full width of the pipe in the both the vertical and horizontal directions because the pipe was not quite round. The results of these measurements can be seen in Figure B.1. It should be noted that for a Reynolds number of approximately  $10^4$ , a pipe length of  $20D$  is necessary to obtain fully developed flow. For our 6 inch diameter duct this length is 10 feet, which was impractical to setup in the lab; therefore the velocity profile measured was not for fully developed flow. The fan was set approximately  $6D$  upstream of the orifice and the velocity profile was measured at approximately  $10D$  downstream.

A volumetric flow rate was determined by integrating the velocity profiles over the duct area. A middle Riemann sum was used for the integration, by taking the average of two adjacent measurements at points 1 and 2 and multiplying by the following differential area:

$$dA = (\pi(3 - x_1)^2 - \pi(3 - x_2)^2) * 0.0254^2 / 2 \quad (\text{B.2})$$

This converts from inches to meters and assumes each velocity measurement is accurate over half the pipe's total area. Because the velocity profile was not symmetric however, an average of the volumetric flow rate, computed from the horizontal and vertical profiles, was used. This is referred to as  $Q_{act}$ .

### Coefficient of Discharge

Once  $Q_{act}$  is known the coefficient of discharge can be found using the pressure difference across the manometer measured with the pressure taps and the following relations.

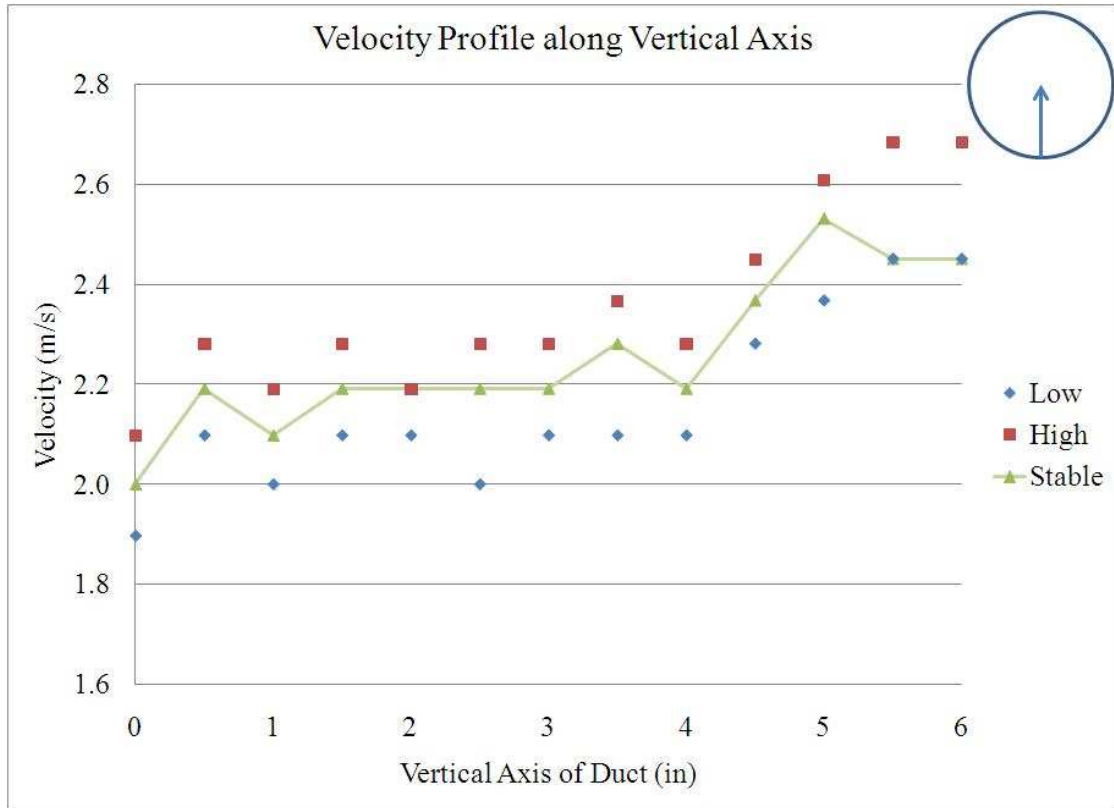


Figure B.1a: Vertical Velocity Profiles in the Orificed Duct

$$Q_{ideal} = \frac{\pi(d_{orifice})^2}{4} \sqrt{\frac{2\Delta P}{\rho(1 - \beta^4)}} \quad (B.3)$$

$$C_0 = \frac{Q_{act}}{Q_{ideal}} \quad (B.4)$$

$$(B.5)$$

Full details of the measurements taken, and calculations performed are included in Figure B.2.

### Inlet Area Flow Rates

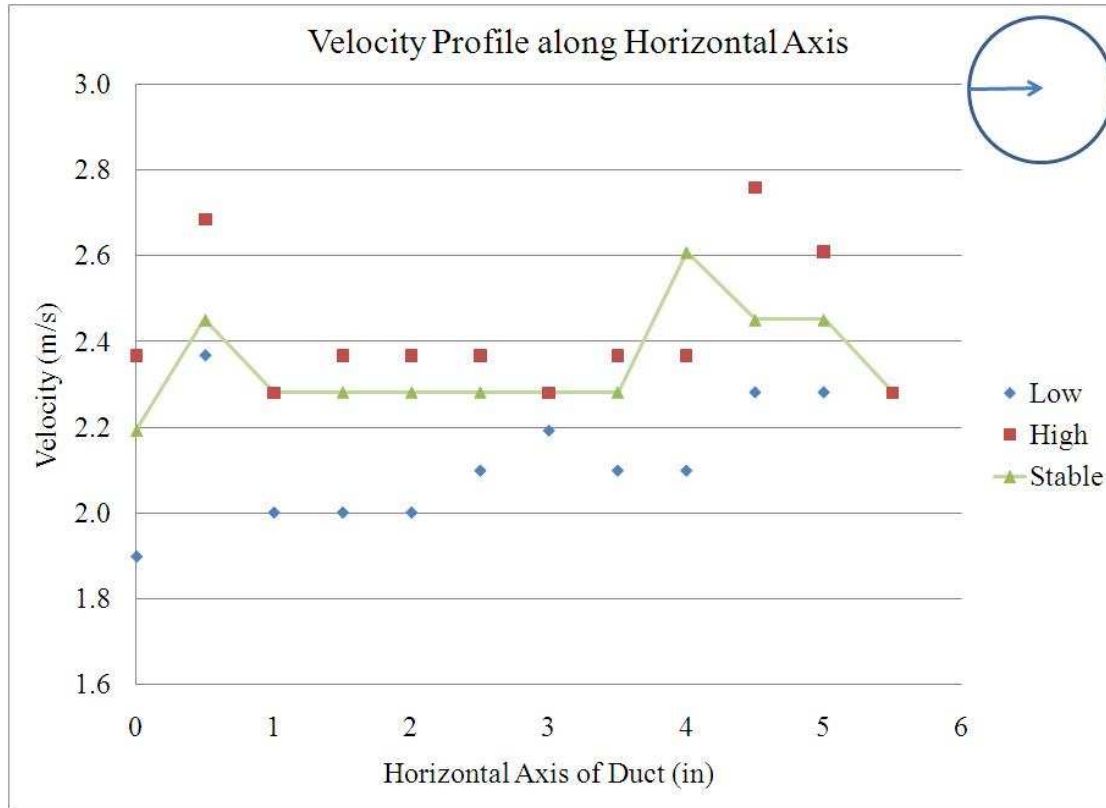


Figure B.1b: Horizontal Velocity Profiles in the Orificed Duct

We also wished to determine how the total volumetric flow to the furnace split amongst the three air inlet areas. For this we used the same pitot tube and equations defined above. In the top port, and secondary ports a flat turbulent profile was assumed so only one measurement was taken in the center of each. For the side ports however we took three measurements along their lengths because of the sharp elbows immediately preceding the air's entrance to the furnace cavity. These are referred to as 'front,' 'center,' and 'back' with 'front' meaning closest to the furnace door. It was assumed that the front and center velocities were each averaged over 40% of the port's area and the back accounted for 10%.

There was quite a bit of room for error during these measurements. The furnace

door remained open during the run thus changing the pressure drop in the furnace. The pitot tube had to be hand held and the manometer readings were fairly unstable as a result. The ultimate goal of the measurements however was to get a feel for how the air split amongst the combustion zones and to get an approximate benchmark for modeling runs. This was accomplished and errors were mitigated by measuring twice to assure the results were adequately repeatable.

Full details of the measurements taken, and calculations performed are included in Figure B.3.

#### Experimental Data: Weight Burned vs. Time

To determine the burn rate, a fourth order polynomial was fit to the experimentally measured weight burned vs. time. This is shown in Figure B.4.

Barometer 30.15 mm Hg Orifice Delta P 0.48 +/-0.03  
 Density 1.244 kg/m3 Q\_ideal 138.4 CFM

Velocity Profile	Flow Rate (CFM)	Accuracy (CFM)	Orifice Coefficient	Accuracy	Calculated Coefficient
Vertical	88	± 3	0.64	± 0.02	0.61
Horizontal	77	± 4	0.56	± 0.04	
Both	75	± 4	0.54	± 0.03	

Measured Quantities					Calculated Quantities					
Vertical	Pressure (in H2O)				Velocity (m/s)					
	Low	High	Stable	Low	High	Stable	Integrate Low	Integrate High	Integrate Stable	
0	0.009	0.011	0.010	1.898	2.099	2.001	0.00557	0.006104	0.005843	
0.5	0.011	0.013	0.012	2.099	2.282	2.192	0.004674	0.005101	0.004892	
1	0.010	0.012	0.011	2.001	2.192	2.099	0.003636	0.003967	0.003805	
1.5	0.011	0.013	0.012	2.099	2.282	2.192	0.002659	0.002834	0.002777	
2	0.011	0.012	0.012	2.099	2.192	2.192	0.001558	0.0017	0.001666	
2.5	0.010	0.013	0.012	2.001	2.282	2.192	0.000519	0.000578	0.000555	
3	0.011	0.013	0.012	2.099	2.282	2.192	0.000532	0.000589	0.000567	
3.5	0.011	0.014	0.013	2.099	2.368	2.282	0.001595	0.001767	0.0017	
4	0.011	0.013	0.012	2.099	2.282	2.192	0.002775	0.002998	0.002888	
4.5	0.013	0.015	0.014	2.282	2.451	2.368	0.004123	0.004487	0.004344	
5	0.014	0.017	0.016	2.368	2.609	2.531	0.005494	0.006036	0.00568	
5.5	0.015	0.018	0.015	2.451	2.685	2.451	0.00683	0.007482	0.00683	
6	0.015	0.018	0.015	2.451	2.685	2.451				
							0.039964	0.043642	0.041548 m3/s	
							85	92	88 CFM	
							0.6120	0.6683	0.6363 C	
							-0.0243	0.0321	range	
Horizontal	Pressure (in H2O)				Velocity (m/s)					
	Low	High	Stable	Low	High	Stable	Integrate Low	Integrate High	Integrate Stable	
0	0.009	0.014	0.012	1.898	2.368	2.192	0.005945	0.00704	0.00647	
0.5	0.014	0.018	0.015	2.368	2.685	2.451	0.004981	0.005662	0.005396	
1	0.010	0.013	0.013	2.001	2.282	2.282	0.003549	0.004123	0.004046	
1.5	0.010	0.014	0.013	2.001	2.368	2.282	0.002535	0.002999	0.00289	
2	0.010	0.014	0.013	2.001	2.368	2.282	0.001558	0.0018	0.001734	
2.5	0.011	0.014	0.013	2.099	2.368	2.282	0.000544	0.000589	0.000578	
3	0.012	0.013	0.013	2.192	2.282	2.282	0.000544	0.000589	0.000578	
3.5	0.011	0.014	0.013	2.099	2.368	2.282	0.001595	0.0018	0.001859	
4	0.011	0.014	0.017	2.099	2.368	2.609	0.002775	0.003247	0.003205	
4.5	0.013	0.019	0.015	2.282	2.758	2.451	0.004046	0.00476	0.004347	
5	0.013	0.017	0.015	2.282	2.609	2.451	0.005203	0.005576	0.005396	
5.5	0.013	0.013	0.013	2.282	2.282	2.282				
							0.033274	0.038185	0.036498 m3/s	
							71	81	77 CFM	
							0.5096	0.5848	0.5589 C	
							-0.0494	0.0258	range	
							<b>Both</b>			
							0.036619	0.040913	0.039023 m3/s	
							78	87	83 CFM	
							0.5608	0.6265	0.5976 C	
							-0.0368	0.0289	range	

Figure B.2: Measurements and calculations for verification of the orifice coefficient of discharge

Barometer 30.15 mm Hg  
Density 1.244 kg/m<sup>3</sup>

Inlet Areas	Test 1		Test 2		Avg	Orifice	Total CFM	71
	Total CFM	79.4	Total CFM	86.9				
Top	43.5	55%	51.2	59%	57%			
Side	33.5	42%	33.5	39%	40%			
Secondary	2.4	3%	2.2	2%	3%			

Primary Chamber											
	Area		4.4 in <sup>2</sup>		Velocity (m/s)				CFM		
Top	0.130	0.18			7.2	8.5			43.5	51.2	
<b>Side</b>											
	Area each			4.1 in <sup>2</sup>		Velocity (m/s)				CFM	Assume front and center each account for 40% of area and back is 10%
	Front	Center	Back	Front	Center	Back	Back				
Front	0.014	0.009	0	2.4	1.9	0		10.3			
Back	0.050	0.066	0	4.5	5.1	0		23.2			
Secondary Chamber											
Secondary Holes											
	Area each		0.37 in <sup>2</sup>		Velocity (m/s)				CFM		
Front	0.002	0.006			0.89	1.55			0.5	0.8	
Back	0.005	0.013			1.42	2.28			0.7	1.2	
Middle Two Holes	CFM										
*Not measured		0.6	0.1								

Figure B.3: Measurements and calculations for the inlet area flow rates in the furnace

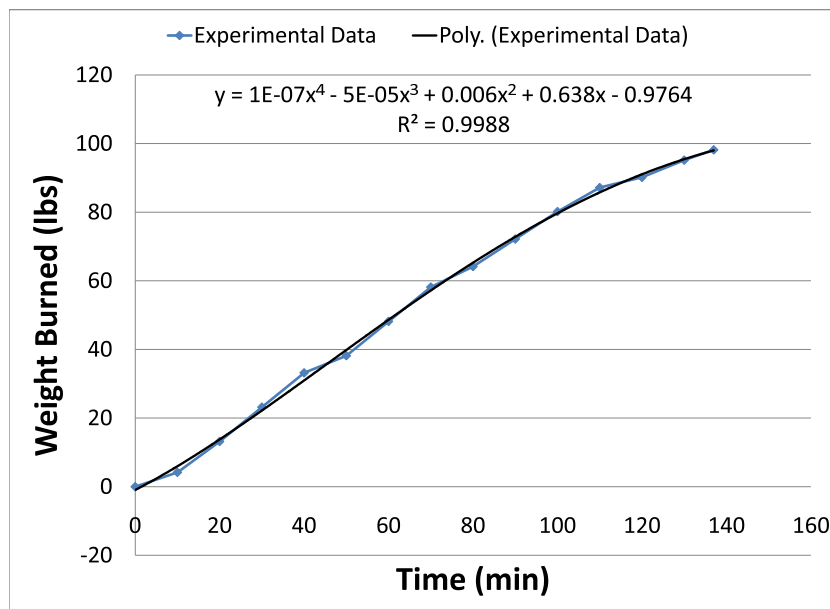


Figure B.4: Experimental data for weight burned vs. time during an EPA test, Category 4 burn



## Appendix C

**BOUNDARY CONDITION CALCULATIONS**

Goal: Determine temperature at the fire brick surface ( $T_s$ ) in the secondary chamber from measured chamber combustion temperatures.

Figure C.1 shows the geometry used for the heat transfer calculation. The heat transfer modes included in the calculation are conduction from the inside to outside of the secondary chamber, convection from the combustion gases and radiation exchange between the gases and brick surface. A full accounting of assumptions and calculations follows.

Assumptions:

- Fire brick surface is gray and diffuse
- Only radiating combustion gases are  $\text{CO}_2$  and  $\text{H}_2\text{O}$
- $\text{CO}_2$  and  $\text{H}_2\text{O}$  partial pressures can be determined from a simple equilibrium calculation
- The gas temperature can be taken as that of the combustion gases in the center of the secondary chamber during a Category IV burn, averaged over the entire run time.
- The secondary chamber is at atmospheric pressure
- The mean beam length ( $L_e$ ) can be approximated as that for infinite parallel planes
- The convective heat transfer coefficient can be approximated as that for turbulent flow over a flat plate.

Conduction

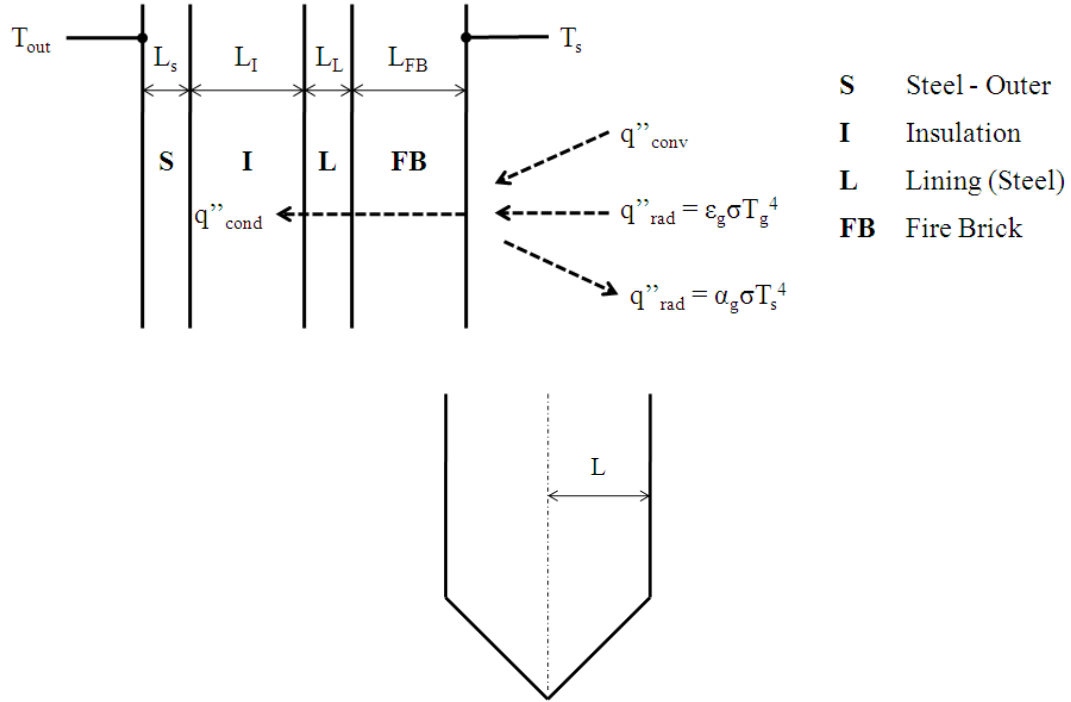


Figure C.1: Relevant geometries (cross section of secondary chamber and chamber wall layers), and a description of heat transfer at the fire brick surface

The conduction component of the heat transfer calculation was determined using a classic thermal resistance model, and the chamber wall description in Figure C.1. A value for  $T_{outer}$  was assumed based on typical observations by the technicians. The resulting equation is given below.

$$q_c'' = \frac{T_s - T_{outer}}{\frac{L_s}{k_s} + \frac{L_I}{k_I} + \frac{L_L}{k_b} + \frac{L_{FB}}{k_{FB}}} \quad (C.1)$$

### Convection

The equation used for heat transfer via convection is given below.

$$q''_{conv} = h(T_g - T_s) \quad (C.2)$$

The convective heat transfer coefficient was determined using an averaged nusselt number correlation for turbulent flow over a flat plate. The chosen correlation is given by Equation C.3 [14].

$$\overline{NU_L} = 0.037Re_L^{4/5} Pr^{1/3} \quad (C.3)$$

### Radiation

The net heat flux due to radiation from a gas to an adjoining surface is given by Equation C.4 [14]. We will use the equations and figures given in Incropera for gaseous emission and absorption to determine  $\varepsilon_g$  and  $\alpha_g$  [14].

$$q''_{rad} = \sigma(\varepsilon_g T_g^4 - \alpha_g T_s^4) \quad (C.4)$$

Total emission and absorption of the combustion gasses are expressed below, where the subscripts  $w$  and  $c$  indicate water vapor and carbon dioxide respectively, and the  $\Delta$  term accounts for the situation where both radiating gases are present. These terms are functions of the partial pressures of the radiating gases, the mean beam length, and the temperatures of both the gas and the surface. The pertinent equations are given below.

Emission

$$\varepsilon_g = \varepsilon_w + \varepsilon_c - \Delta\varepsilon \quad (C.5)$$

$$\varepsilon_w = f(T_g, p_w L_e)$$

$$\varepsilon_c = f(T_g, p_c L_e)$$

$$\Delta\varepsilon = f(p_w/(p_c + p_w), T_g, L_e(p_w + p_c))$$

Absorption

$$\alpha_g = \alpha_w + \alpha_c - \Delta\alpha \quad (C.6)$$

Correlations for absorptivity of radiating gasses

$$\alpha_w = C_w \left( \frac{T_g}{T_s} \right)^{0.45} * \varepsilon_w \left( T_s, p_w L_e \frac{T_s}{T_g} \right) \quad (\text{C.7})$$

$$\alpha_c = C_c \left( \frac{T_g}{T_s} \right)^{0.65} * \varepsilon_c \left( T_s, p_c L_e \frac{T_s}{T_g} \right) \quad (\text{C.8})$$

$$\Delta\alpha = \Delta\varepsilon \quad (\text{C.9})$$

### Energy Conservation

With the following energy conservation equation we can now iterate to solve for  $T_s$ .

$$q_c'' = q_{rad}'' + q_{conv}'' \quad (\text{C.10})$$

A cursory sensitivity study was conducted and it was found that the solution for  $T_s$  was not very sensitive to the values of the convective heat transfer coefficient and outer chamber temperature. A 200% change in either of these values caused no more than a 2% change in the value of  $T_s$ .

Goal: Determine boundary condition values for  $k$  and  $\epsilon$  when using the  $k - \epsilon$  turbulence model.

The turbulent intensity ( $I$ ) and the turbulent length scale ( $l$ ) for fully developed flow in a duct are defined by the following empirical relationships where  $L = D_H$ , the hydraulic diameter [2].

$$I \equiv \frac{u'}{u_{avg}} = 0.16(Re_{D_H})^{(-1/8)} \quad (\text{C.11})$$

$$l = 0.07L = 0.07D_H \quad (\text{C.12})$$

From these quantities the turbulent kinetic energy and dissipation rate can be calculated where  $C_\mu$  is an empirical constant approximately 0.09 [2].

$$k = \frac{3}{2}(u_{avg}I)^2 \quad (\text{C.13})$$

$$\epsilon = C_{\mu}^{3/4} \frac{k^{3/2}}{l} \quad (\text{C.14})$$